



MIT Open Access Articles











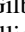

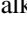
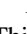



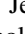
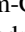

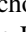

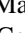
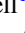




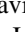

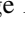
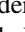


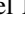
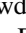
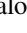


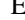


Two Young Planetary Systems around Field Stars with Ages between 20 and 320 Myr from TESS

The MIT Faculty has made this article openly available. **Please share** how this access benefits you. Your story matters.

As Published	10.3847/1538-3881/ABBA22
Publisher	American Astronomical Society
Version	Final published version
Citable link	https://hdl.handle.net/1721.1/135592
Terms of Use	Article is made available in accordance with the publisher's policy and may be subject to US copyright law. Please refer to the publisher's site for terms of use.



Two Young Planetary Systems around Field Stars with Ages between 20 and 320 Myr from TESS

George Zhou^{1,28} , Samuel N. Quinn¹ , Jonathan Irwin¹, Chelsea X. Huang² , Karen A. Collins¹ , Luke G. Bouma³ , Lamisha Khan^{1,4}, Anaka Landrigan^{1,4}, Andrew M. Vanderburg⁵ , Joseph E. Rodriguez¹ , David W. Latham¹ , Guillermo Torres¹ , Stephanie T. Douglas¹ , Allyson Bieryla¹ , Gilbert A. Esquerdo¹ , Perry Berlind¹, Michael L. Calkins¹ , Lars A. Buchhave⁶ , David Charbonneau¹ , Kevin I. Collins⁷ , John F. Kielkopf⁸ , Eric L. N. Jensen⁹ , Thiam-Guan Tan¹⁰ , Rhodes Hart¹¹, Brad Carter¹¹, Christopher Stockdale¹² , Carl Ziegler¹³ , Nicholas Law¹⁴ , Andrew W. Mann¹⁴ , Steve B. Howell¹⁵ , Rachel A. Matson^{15,16} , Nicholas J. Scott¹⁵ , Elise Furlan¹⁷ , Russel J. White¹⁸ , Coel Hellier¹⁹ , David R. Anderson^{19,20} , Richard G. West²⁰, George Ricker² , Roland Vanderspek² , Sara Seager^{2,21,22} , Jon M. Jenkins¹⁵ , Joshua N. Winn³ , Ismael Mireles² , Pamela Rowden²³ , Daniel A. Yahalom¹ , Bill Wohler^{24,25} , Clara E. Brasseur²⁶ , Tansu Daylan² , and Knicole D. Colón²⁷ 

¹ Center for Astrophysics, Harvard & Smithsonian, 60 Garden Street, Cambridge, MA 02138, USA; george.zhou@cfa.harvard.edu

² Department of Physics, and Kavli Institute for Astrophysics and Space Research, Massachusetts Institute of Technology, Cambridge, MA 02139, USA

³ Department of Astrophysical Sciences, Princeton University, NJ 08544, USA

⁴ Cambridge Rindge and Latin High School, USA

⁵ Department of Astronomy, The University of Texas at Austin, Austin, TX 78712, USA

⁶ DTU Space, National Space Institute, Technical University of Denmark, Elektrovej 328, DK-2800 Kgs. Lyngby, Denmark

⁷ George Mason University, 4400 University Drive, Fairfax, VA 22030, USA

⁸ Department of Physics and Astronomy, University of Louisville, Louisville, KY 40292, USA

⁹ Department of Physics & Astronomy, Swarthmore College, Swarthmore, PA 19081, USA

¹⁰ Perth Exoplanet Survey Telescope, Perth, WA, Australia

¹¹ Centre for Astrophysics, University of Southern Queensland, Toowoomba, QLD, 4350, Australia

¹² Hazelwood Observatory, VIC, Australia

¹³ Dunlap Institute for Astronomy and Astrophysics, University of Toronto, 50 St. George Street, Toronto, ON M5S 3H4, Canada

¹⁴ Department of Physics and Astronomy, The University of North Carolina at Chapel Hill, Chapel Hill, NC 27599-3255, USA

¹⁵ NASA Ames Research Center, Moffett Field, CA 94035, USA

¹⁶ U.S. Naval Observatory, Washington, DC 20392 USA

¹⁷ NASA Exoplanet Science Institute, Caltech/IPAC, Mail Code 100-22, 1200 East California Boulevard, Pasadena, CA 91125, USA

¹⁸ IPAC, Mail Code 314-6, Caltech, 1200 East California Boulevard, Pasadena, CA 91125, USA

¹⁹ Astrophysics Group, Keele University, Staffordshire, ST5 5BG, UK

²⁰ Department of Physics, University of Warwick, Gibbet Hill Road, Coventry CV4 7AL, UK

²¹ Department of Earth, Atmospheric and Planetary Sciences, Massachusetts Institute of Technology, Cambridge, MA 02139, USA

²² Department of Aeronautics and Astronautics, MIT, 77 Massachusetts Avenue, Cambridge, MA 02139, USA

²³ School of Physical Sciences, The Open University, Milton Keynes MK7 6AA, UK

²⁴ NASA Ames Research Center, Moffett Field, CA 94035, USA

²⁵ SETI Institute, Mountain View, CA 94043, USA

²⁶ Space Telescope Science Institute, USA

²⁷ NASA Goddard Space Flight Center, Exoplanets and Stellar Astrophysics Laboratory (Code 667), Greenbelt, MD 20771, USA

Received 2020 July 27; revised 2020 September 11; accepted 2020 September 19; published 2020 December 2

Abstract

Planets around young stars trace the early evolution of planetary systems. We report the discovery and validation of two planetary systems with ages $\lesssim 300$ Myr from observations by the Transiting Exoplanet Survey Satellite (TESS). The 40–320 Myr old G star TOI-251 hosts a $2.74^{+0.18}_{-0.18} R_{\oplus}$ mini-Neptune with a 4.94 day period. The 20–160 Myr old K star TOI-942 hosts a system of inflated Neptune-sized planets, with TOI-942b orbiting in a period of 4.32 days with a radius of $4.81^{+0.20}_{-0.20} R_{\oplus}$ and TOI-942c orbiting in a period of 10.16 days with a radius of $5.79^{+0.19}_{-0.18} R_{\oplus}$. Though we cannot place either host star into a known stellar association or cluster, we can estimate their ages via their photometric and spectroscopic properties. Both stars exhibit significant photometric variability due to spot modulation, with measured rotation periods of ~ 3.5 days. These stars also exhibit significant chromospheric activity, with age estimates from the chromospheric calcium emission lines and X-ray fluxes matching that estimated from gyrochronology. Both stars also exhibit significant lithium absorption, similar in equivalent width to well-characterized young cluster members. TESS has the potential to deliver a population of young planet-bearing field stars, contributing significantly to tracing the properties of planets as a function of their age.

Unified Astronomy Thesaurus concepts: [Exoplanet evolution \(491\)](#); [Exoplanets \(498\)](#)

1. Introduction

The first few hundred million yr of planet evolution sculpts the population of exoplanetary systems we observe today. The properties of young planetary systems help unravel the factors

that shape the present-day population: in situ formation, migration, and photoevaporation. Probing the timescales of these mechanisms motivates us to search for planets within the first few hundred million yr of their birth.

Recent searches for young planets have yielded a handful of discoveries with targeted radial velocity surveys and space-based

²⁸ Hubble Fellow.

transit monitoring. Dozens of planets have been identified in the 600–800 Myr old Praesepe and Hyades clusters (Quinn et al. 2012, 2014; Mann et al. 2016a, 2017, 2018; Obermeier et al. 2016; Ciardi et al. 2018; Livingston et al. 2018, 2019; Rizzuto et al. 2018; Vanderburg et al. 2018). These discoveries enabled estimates of planet occurrence rates in million yr old cluster environments (e.g., Rizzuto et al. 2017).

To sample the earlier stages of planet evolution, transit searches have focused on members of known young stellar associations, finding planets with ages ranging from ~ 10 to 150 Myr. Observations from the K2 mission revealed planets within the Upper Scorpius moving group (David et al. 2016; Mann et al. 2016b) and Taurus-Auriga star-forming region (David et al. 2019a, 2019b).

With the library of all-sky photometry made available by the Transiting Exoplanet Survey Satellite (TESS; Ricker et al. 2016), planets around bright young stars have been identified (e.g., Newton et al. 2019; E. R. Newton et al. 2020, in preparation; Mann et al. 2020; Plavchan et al. 2020; Rizzuto et al. 2020). These are the first planets around bright young stars that are suitable for in-depth characterizations, enabling the first obliquity measurements of newly formed planets (Montet et al. 2020; Zhou et al. 2020), as well as atmospheric studies in the near future.

However, star-forming clusters begin to disperse within the first hundred million yr of formation (Krumholz et al. 2019). Left behind are relatively young stars that can no longer be traced back to their source of origin. These stars can still be identified by their signatures of youth. Mamajek & Hillenbrand (2008) summarized the activity signatures that can be used to provide approximate ages of Sun-like stars. The rapid rotation of these young stars leads to enhanced chromospheric activity and X-ray emission. Their current rotation rates can help guide the age estimates via gyrochronology. The abundance of lithium in the atmospheres of main-sequence Sun-like stars is also a useful youth indicator. Recent efforts to trace young field stars have made use of all-sky spectroscopic surveys to catalog large numbers of chromospherically active (e.g., Žerjal et al. 2013) and lithium-bearing (e.g., Žerjal et al. 2019) stars.

These photometric and spectroscopic signatures of youth, however, are often detrimental to our ability to identify and characterize the planets these stars harbor. The photometric variations due to star spots and stellar rotation make transit planet searches more difficult. The same spot activity induces radial velocity variations on the ~ 100 m s $^{-1}$ level, masking the planetary orbits. Despite these difficulties, Sanchis-Ojeda et al. (2013) identified Kepler-63 b as a giant planet around an ~ 300 Myr young field star and made use of the spot activity to infer its orbital obliquity via transit spot-crossing events. The small planets around K2-233 (David et al. 2018a) and EPIC 247267267 (David et al. 2018b) are additional examples of young field stars with ages of 100–700 Myr discovered by the K2 mission.

We report the discovery of a mini-Neptune around TOI-251, which we determine to have an age of 40–320 Myr based on its rotational, spectroscopic, and X-ray properties. We also report the discovery of two inflated Neptunes around TOI-942, with ages of 20–160 Myr, as measured from the host star’s rotation, spectroscopic, and X-ray age indicators. These planets were validated by a campaign of ground-based photometric and spectroscopic observations. In particular, the ability to predict future transit times degraded substantially over the year

between the TESS discovery and subsequent follow-up efforts. Our ground-based photometric follow-up campaign demonstrates the effectiveness of small telescopes in recovering the shallow 1 mmag transits that these small planets exhibit. These young planets around field stars open an untapped population that can help us construct the properties of planetary systems over time.

2. Candidate Identification and Follow-up Observations

2.1. Identification of Planet Candidates by TESS

During Sector 2, between 2018 August 8 and September 9, TIC 224225541 received TESS 2 minute cadenced target pixel stamp observations as part of the TESS Candidate Target List (CTL; Stassun et al. 2018), with the target star being located on Camera 2, CCD 4 of the TESS array. Light curves and transit identification were made possible via the Science Processing Observation Center (SPOC; Jenkins et al. 2016). The transits of the mini-Neptune were detected as per Twicken et al. (2018) and Li et al. (2019), with a multiple event statistic of 10.9, and released to the community as TOI-251b, with an orbital period of 4.94 days. We make use of the simple aperture photometry made available for this star for further analysis (Twicken et al. 2010; Morris et al. 2020). The TESS light curve of TOI-251 is shown in Figure 1, and individual transits of TOI-251b are shown in Figure 2.

During Sector 5 of the primary mission, between 2018 November 15 and December 11, TIC 146520535 was observed by the Camera 2 CCD 2 full-frame images (FFIs) at 30 minute cadence. The MIT quick-look pipeline (Huang et al. 2019) identified a set of transit events at 4.331 days with a signal-to-noise ratio of 11.7 and released as TOI-942b. In subsequent visual examinations of the light curves, two single transits of slightly deeper depth than TOI-942b were identified in the light curves spaced 10.16 days apart. Further analysis showed that these two single transits are identical in depth and duration and due to a second planet candidate, TOI-942c.

We then extracted the light curves for TOI-942 from the public FFIs made available on the MAST archive using the *lightkurve* package (Barentsen et al. 2019). A 10×10 pixel FFI cutout was extracted around the target star using the TESScut function (Brasseur et al. 2019). The photometric aperture was defined to encompass the brightest 68% of pixels within a maximum radius of 3 pixels from the target star coordinates. Surrounding pixels without nearby stars are used for background subtraction. The TESS light curve of TOI-942 is shown in Figure 3, and individual transits of TOI-942b and c are shown in Figures 4 and 5, respectively.

2.2. Spectroscopic Follow-up

2.2.1. SMARTS 1.5 m/CHIRON

We obtained a series of spectroscopic observations with the CHIRON facility to characterize the host star properties and constrain the masses of the planets in each system. CHIRON is a high-resolution spectrograph on the 1.5 m SMARTS telescope, located at Cerro Tololo Inter-American Observatory (CTIO), Chile (Tokovinin et al. 2013). CHIRON is fed through an image slicer via a fiber, yielding a spectral resolving power of $\lambda/\Delta\lambda \equiv R = 80,000$ over the wavelength region 4100–8700 Å.

Radial velocities were extracted from CHIRON spectra by fitting the line profiles derived from each spectra. The line

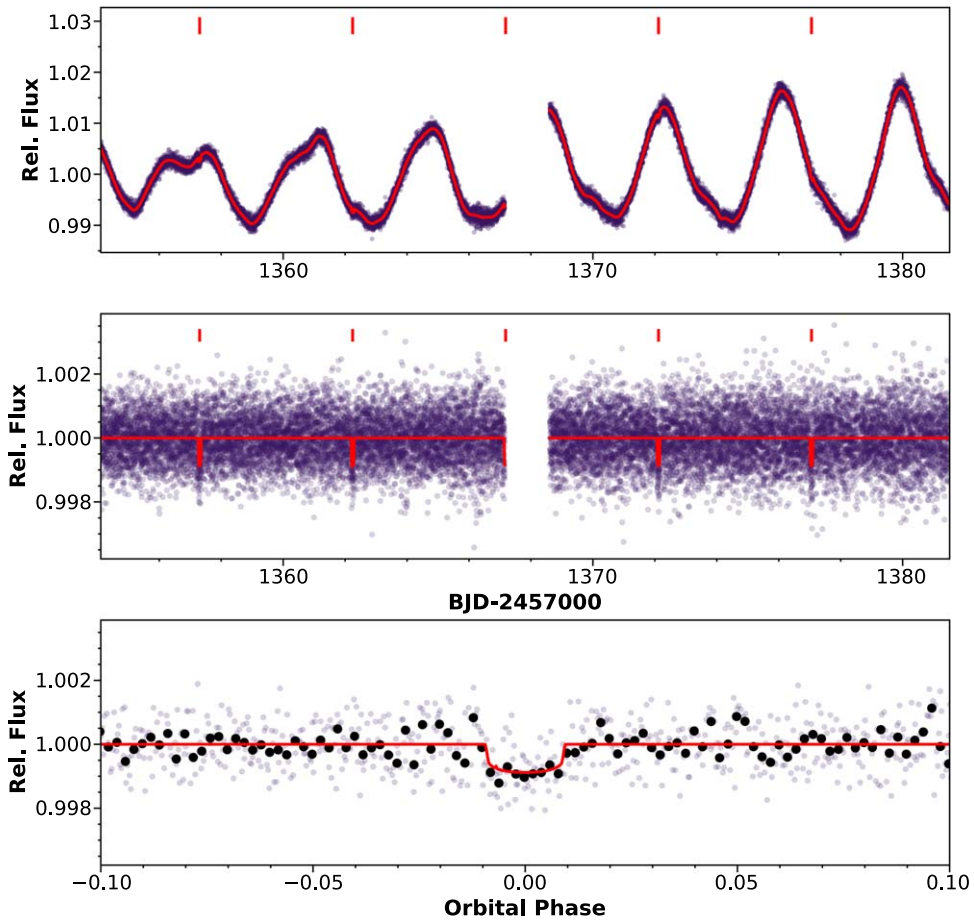


Figure 1. Full TESS light curve of TOI-251 during Sector 2 of short-cadence observations. The top panel shows the SPOC simple aperture photometry fluxes. The red ticks above the light curve mark the times of transit for TOI-251b. The middle panel shows the light curve after removal of the stellar activity signal as modeled via our global analysis. The bottom panel shows the phased light curve around the transit of TOI-251b. The black points show the binned light curve at phase intervals of 0.002. The best-fit models are shown in red in each panel.

profiles are measured via a least-squares deconvolution of the observed spectra against synthetic templates (following Donati et al. 1997), listed in Tables 1 and 2, and plotted in Figures 6 and 7.

In addition to providing radial velocity and stellar atmosphere parameter measurements, the CHIRON spectra also allow us to search for additional blended spectral companions that may be indicative of other astrophysical false-positive scenarios for these systems. We perform a signal injection and recovery exercise to determine the detection thresholds for any additional spectroscopic stellar companion that may be blended in the spectrum. The detectability of the blended source is determined by its flux ratio and velocity separation to the target star and its rotational broadening. As such, we performed $\sim 10,000$ iterations of the injection, with different combinations of these factors, to the averaged spectroscopic line profile for each target star. The derived detection thresholds are shown in Figure 8. We can rule out any nonassociated stellar companions with $\Delta\text{mag} < 4$ for TOI-251, assuming they exhibit minimal rotational broadening and substantial velocity separation between the target star and the blended companion. Similarly, we can rule out blended, nonassociated, slowly rotating stellar companions with $\Delta\text{mag} < 3.5$ for TOI-942. Our ability to detect such companions degrades significantly if they are rapidly rotating or have similar systemic velocities to the target star.

We also made use of the CHIRON observations to measure the projected rotational velocity $v \sin I_*$ of the host stars. Following Zhou et al. (2018), we model the line profiles derived from the CHIRON spectra via a convolution of kernels representing the rotation, radial-tangential macroturbulence, and instrument broadening terms. The rotational and radial-tangential macroturbulence kernels follow the prescription in Gray (2005), while the instrument broadening kernel is represented by a Gaussian function of width that of the instrument resolution. For TOI-251, we measured a projected rotational broadening velocity of $v \sin I_* = 11.5 \pm 1.0 \text{ km s}^{-1}$ and a macroturbulent velocity of $v_{\text{mac}} = 7.9 \pm 1.0 \text{ km s}^{-1}$. For TOI-942, we measure $v \sin I_* = 14.3 \pm 0.5 \text{ km s}^{-1}$ and $v_{\text{mac}} = 9.8 \pm 3.4 \text{ km s}^{-1}$. We note that for slowly rotating stars, there is a significant degeneracy between various line broadening parameters. These degeneracies can systematically impact future observations, such as transit spectroscopic obliquity observations or estimates of the line-of-sight inclination of the system.

2.2.2. FLWO 1.5 m TRES

We also obtained observations of TOI-251 and TOI-942 with the Tillinghast Reflect Echelle Spectrograph (TRES; Fűrész 2008) on the 1.5 m reflector at the Fred Lawrence Whipple Observatory (FLWO), Arizona, USA. TRES is a

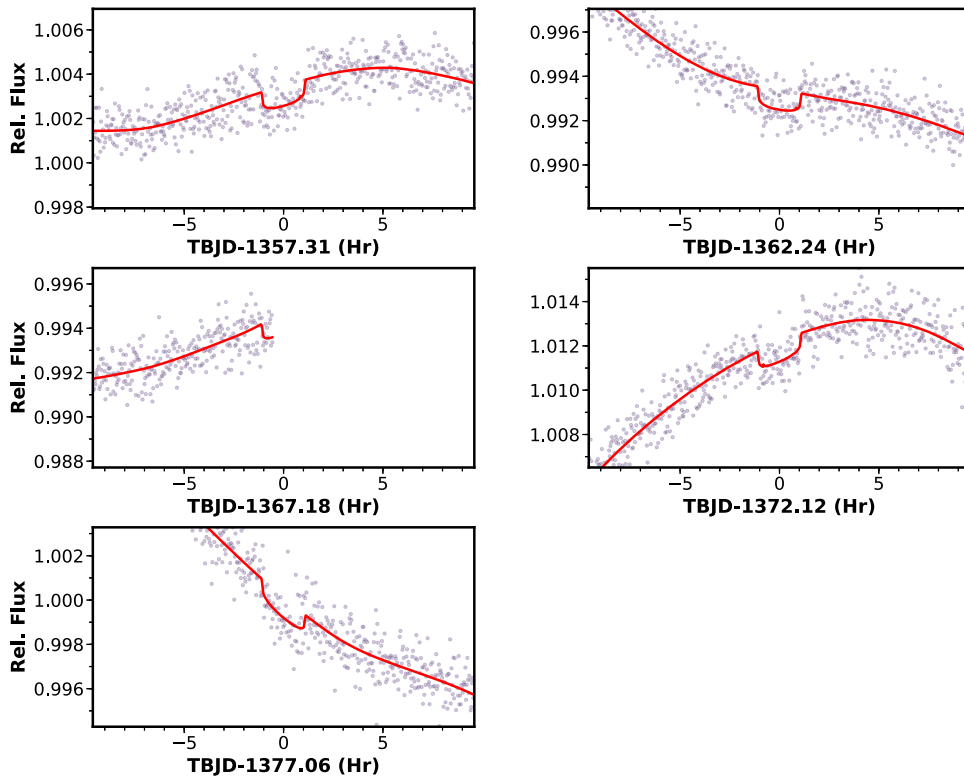


Figure 2. Individual transits of TOI-251b during the TESS observations. Each panel shows an individual transit, with the mid-transit epoch labeled on the X-axis. The best-fit model is overlaid in red, showing the transit and stellar activity models.

fiber-fed echelle spectrograph with a resolution of $R \sim 44,000$ over the spectral region of 3850–9100 Å. The observing strategy and reduction procedure are outlined in Buchhave et al. (2012).

One observation was obtained for TOI-251, and two were obtained for TOI-942. These spectra were used to measure the stellar atmospheric properties of the host stars via the Stellar Parameter Classification pipeline (Buchhave et al. 2010), subsequently used as priors in our global analyses (Section 5). We find TOI-251 to have a Sun-like stellar surface effective temperature of $T_{\text{eff}} = 5833 \pm 143$ K, surface gravity of $\log g = 4.49 \pm 0.23$ dex, and metallicity of $[m/H] = -0.16 \pm 0.13$ dex. The early K star TOI-942 has $T_{\text{eff}} = 5187 \pm 52$ K, $\log g = 4.59 \pm 0.10$ dex, and $[m/H] = 0.07 \pm 0.08$ dex.

2.3. Photometric Follow-up

We obtained a series of ground-based photometric follow-up observations to confirm that the transits are on target, eliminate false-positive scenarios, and refine the ephemeris and orbital parameters.

Full and partial transits of TOI-251b, TOI-942b, and TOI-942c were obtained by an array of ground-based observatories. In particular, with only two transits in the TESS observations, the ephemeris uncertainty for TOI-942c was as large as 5 hr, while the uncertainties for the shorter-period planets TOI-251b and TOI-942b were 2 hr. The first attempts at recovering the transits of both planets failed due to these large uncertainties but were still useful in refining the transit predictions. Subsequent attempts fortuitously captured partial transits, leading to the recovery of the ephemeris. The ground-based follow-up light curves of TOI-251 and TOI-942 are shown in Figures 9 and 10, respectively.

2.3.1. Las Cumbres Observatory

The Las Cumbres Observatory Global Telescope (LCOGT) is a global network of small robotic telescopes (Brown et al. 2013). A full transit of TOI-251b was observed by the 1 m LCOGT telescope located at Siding Spring Observatory, Australia. The observations are scheduled via the TESS Transit Finder, which is a customized version of the Tapir software package (Jensen 2013). The observations were obtained with the Sinistro camera in the Y band on the night of 2019 July 23. The LCOGT images were calibrated by the standard LCOGT BANZAI pipeline (McCully et al. 2018), and the photometric data were extracted using the Astro-ImageJ (AIJ) software package (Collins et al. 2017), showing a likely detection of the 1 mmag transit event. Nearby stars were cleared for signs of eclipsing binaries, showing that the transit event is on target to within seeing limits. The observation is shown in Figure 9.

2.3.2. Mt. Kent Observatory

A full transit of TOI-251b was observed with the University of Louisville Research Telescope at Mt. Kent Observatory, Queensland, Australia. The University of Louisville Research Telescope is a PlaneWave Instruments CDK700 0.7 m telescope equipped with a $4K \times 4K$ detector. The observation on 2019 July 28 was obtained in the i' band, spanning 4 hr, with an average exposure time of ~ 90 s. Photometry was extracted using AIJ (Collins et al. 2017), showing a successful detection of the transit event. The nearby stars were again checked for signatures of eclipsing binaries, with none detected.

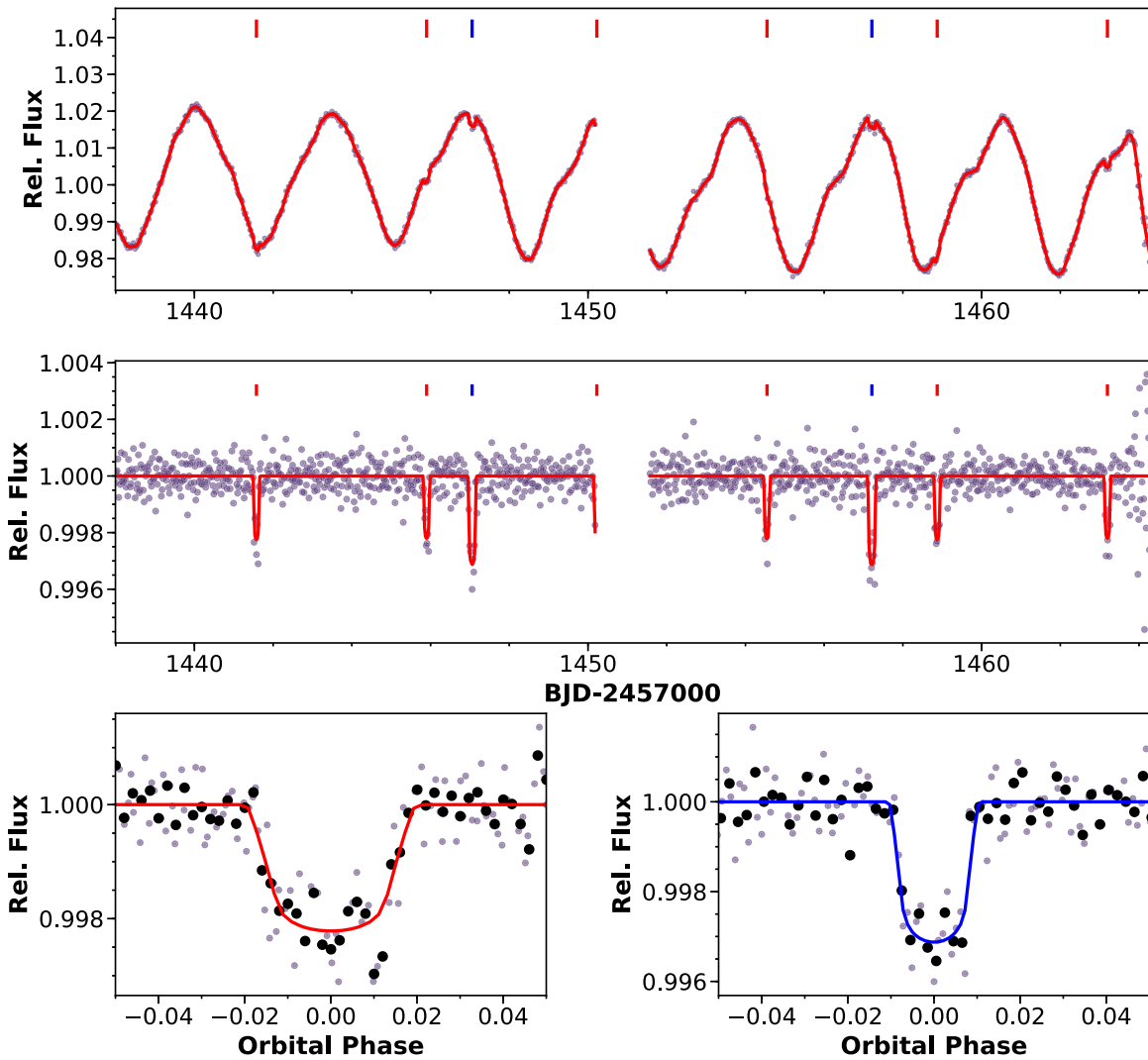


Figure 3. TESS light curve of TOI-942 from 30 minute cadence FFIs during Sector 5 of observations. The panels are arranged the same as Figure 1. The red ticks above the light curve mark the times of transit for TOI-942b, and the blue ticks mark the transit times for TOI-942c. The phase-folded transit of TOI-942b is shown on the bottom left, and TOI-942c is shown on the bottom right. The black points show the binned light curve at phase intervals of 0.002.

2.3.3. M_{Earth}

The M_{Earth} instruments are described in detail by Irwin et al. (2015), and for brevity, we do not repeat those details here.

For the majority of the M_{Earth} observations listed in Table 3, we adopted a standard observational strategy used for bright TOIs where all but one of the available telescopes at a given observing site are operated defocused to obtain photometry of the target star, and one telescope observes in focus with the target star saturated to obtain photometry of any nearby contaminating stars not properly resolved in the defocused observations. Once these stars had been fully ruled out as the source of the transits, we simply used all telescopes in defocused mode to obtain a slight improvement in sampling. This was done for the observation of TOI-251 and the last two observations of TOI-942 (2019 December 5 and 26) only.

With the exception of the observation of TOI-251 on 2019 November 17, which was gathered from both M_{Earth}-North and M_{Earth}-South simultaneously (using a total of 15 telescopes, eight at M_{Earth}-North and seven at M_{Earth}-South), all other observations were gathered from M_{Earth}-South using

seven telescopes. For TOI-942, the exposure times were 60 s on all telescopes, and the defocused telescopes used a half-flux diameter (HFD) of 12 pixels. For TOI-942, we used a defocus setting of 6 pixels HFD and an exposure time of 60 s for the defocus telescopes and 30 s for the single in-focus telescope at M_{Earth}-South, as well as 8 pixels HFD with all telescopes using 60 s exposure times at M_{Earth}-North. These instruments use a different model of CCD and so have different pixel scales ($0''.84 \text{ s}^{-1}$ at M_{Earth}-South and $0''.76 \text{ s}^{-1}$ at M_{Earth}-North) and require slightly different observational setups to achieve the same saturation limit.

Data were gathered continuously subject to twilight, zenith distance, and weather constraints. Telescope 7 at M_{Earth}-South used in the defocus ensemble had a shutter stuck in the open position for all observations, but this does not appear to affect the light curves despite visible smearing during readout. All data were reduced following standard procedures detailed in Irwin et al. (2007) and Berta et al. (2012). Photometric aperture radii for extraction of the defocus time series of the target star were 24 pixels for TOI-251, 9.9 pixels for TOI-942 at M_{Earth}-South, and 12.7 pixels for TOI-251 at M_{Earth}-North.

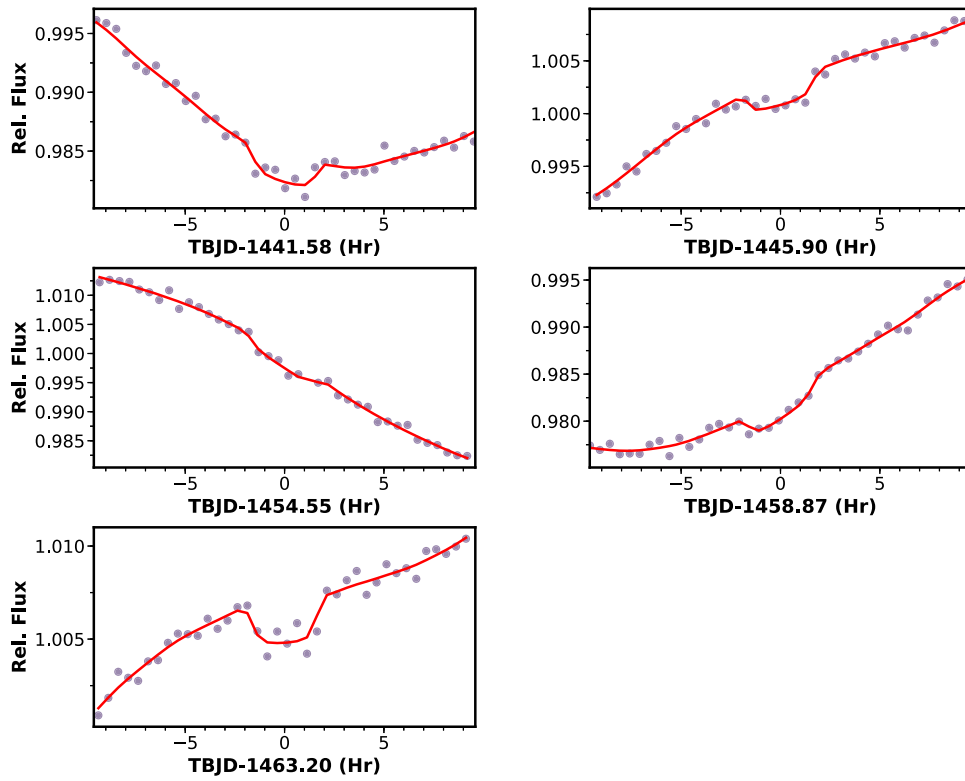


Figure 4. Individual transits of TOI-942b during the TESS observations. Each panel shows an individual transit, with hours from the mid-transit epoch labeled. The best-fit model is overlaid in red, showing the transit and stellar activity models. Note that the vertical scales differ from transit to transit due to the sharply varying stellar activity at each transit event.

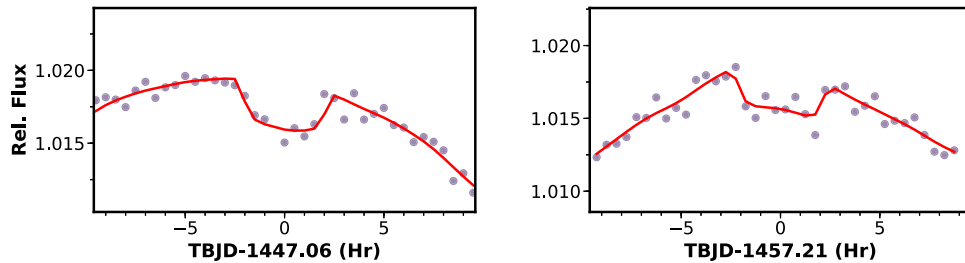


Figure 5. Individual transits of TOI-942c during the TESS observations. Each panel shows an individual transit. The best-fit model is overlaid in red, showing the transit and stellar activity models.

Table 1
Radial Velocities for TOI-251

BJD-TDB	RV (km s ⁻¹)	RV Error (km s ⁻¹)	Inst.
2,458,472.59427	-2.323	0.031	TRES
2,458,636.91068	-2.087	0.013	CHIRON
2,458,637.92204	-1.933	0.019	CHIRON
2,458,640.90185	-2.058	0.024	CHIRON
2,458,650.86649	-2.087	0.018	CHIRON
2,458,653.83789	-2.188	0.050	CHIRON
2,458,665.79446	-2.134	0.013	CHIRON
2,458,666.84512	-2.004	0.010	CHIRON
2,458,667.86580	-2.080	0.006	CHIRON
2,458,668.80856	-1.983	0.019	CHIRON

Table 2
Radial Velocities for TOI-942

BJD-TDB	RV (km s ⁻¹)	RV Error (km s ⁻¹)	Inst.
2,458,579.51343	25.400	0.024	CHIRON
2,458,751.87828	25.467	0.043	CHIRON
2,458,774.79336	25.197	0.038	CHIRON
2,458,775.80474	25.147	0.043	CHIRON
2,458,782.85938	25.518	0.031	CHIRON
2,458,785.79240	25.493	0.044	CHIRON
2,458,787.72494	25.294	0.026	CHIRON
2,458,789.71153	25.310	0.036	CHIRON
2,458,791.77641	25.240	0.033	CHIRON
2,458,775.91595	25.181	0.267	TRES
2,458,786.92907	25.024	0.074	TRES

2.3.4. WASP Archival Observations

Multiseason monitoring by ground-based transit surveys was also received by TOI-251 and TOI-942. The Wide Angle Search for Planets (WASP) Consortium (Pollacco et al. 2006)

observed both target stars with the Southern SuperWASP facility, located at the Sutherland Station of the South African Astronomical Observatory. Each SuperWASP station consists

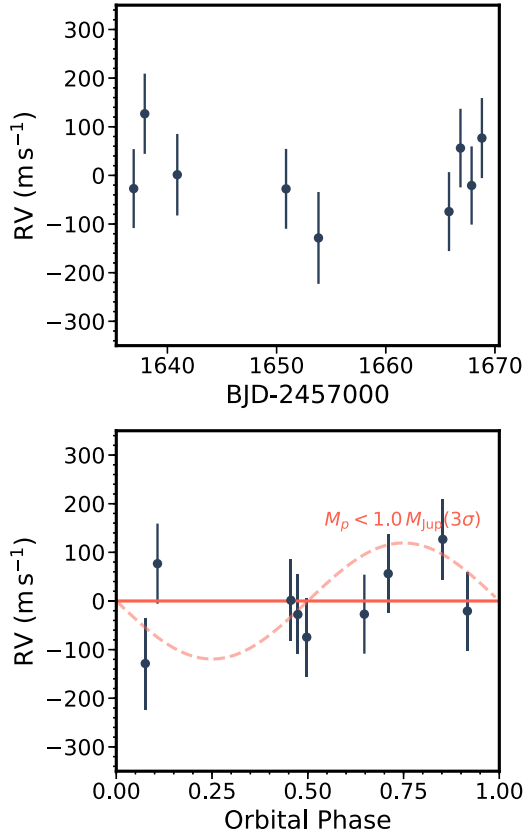


Figure 6. Radial velocities of TOI-251 obtained with CHIRON. The top panel shows the radial velocities as a function of their observation. The plotted uncertainties are the quadrature addition of the per-point measurement uncertainty and stellar jitter. The bottom panel shows the velocities phase-folded to the period of TOI-251b, with the transit occurring at phase 0. The dashed radial velocity model shows the 3σ mass upper limit that we can place on TOI-251b based on these velocities.

of arrays of eight commonly mounted 200 mm $f/1.8$ Canon telephoto lenses equipped with a $2K \times 2K$ detector yielding a field of view of $7^\circ 8' \times 7^\circ 8'$ camera $^{-1}$.

WASP observations of TOI-251 and TOI-942 spanned 8 yr, from 2006 to 2014. The $\sim 2\%$ spot modulation signal is clear in the WASP data sets for both host stars. We make use of these observations in Section 4 to confirm that the rotation period we measure from TESS is robust and consistent with that seen over the significantly longer timescales of the WASP observations.

2.4. High Spatial Resolution Imaging

We obtained a series of high spatial resolution imagery of the target stars to check for blended nearby stellar companions. Such companions can be the source of false-positive signals due to stellar eclipsing binaries or dilute the planetary transit signal leading to systematically smaller planet radius measurements.

Observations of TOI-251 and TOI-942 were obtained as part of the Southern Astrophysical Research (SOAR) TESS survey (Ziegler et al. 2020). Speckle imaging observations were obtained with the Andor iXon-888 camera on the 4.1 m SOAR telescope. Observations of TOI-251 were obtained on 2019 May 18 and TOI-942 on 2019 November 19. Each target star observation involved 400 frames of 200×200 binned pixels about the target with a pixel scale of $0''.01575$ obtained over the course of 11 s. The observations were reduced per Tokovinin (2018). The

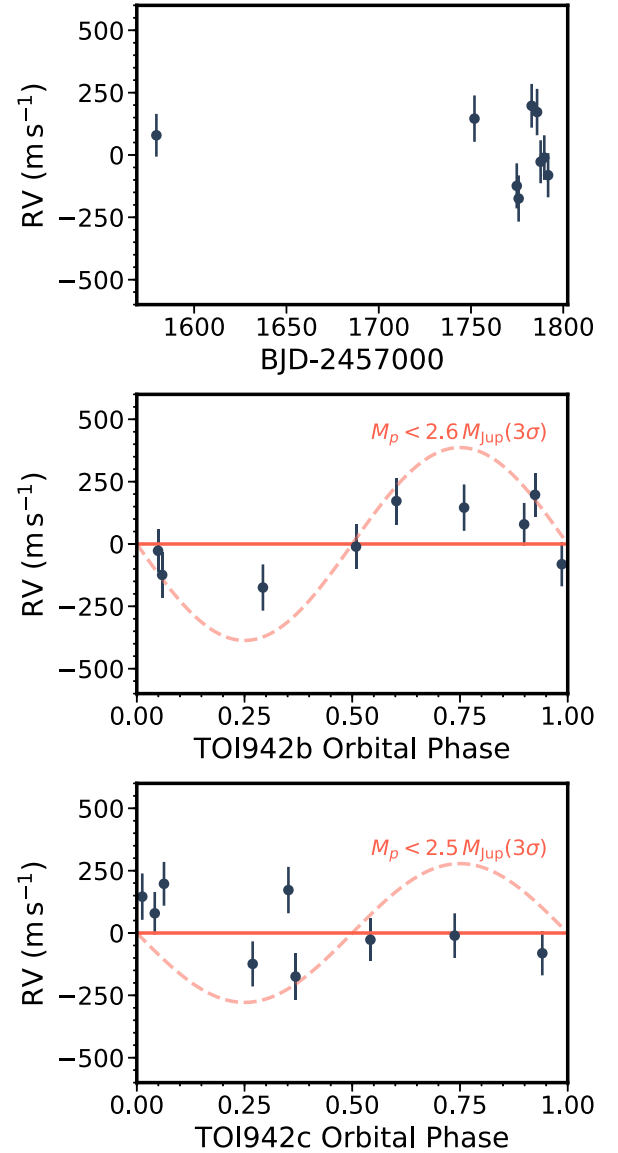


Figure 7. Radial velocities of TOI-942 obtained with CHIRON. The top panel shows the radial velocities as a function of their observation. The plotted uncertainties are the quadrature addition of the per-point measurement uncertainty and stellar jitter. The middle and bottom panels show the velocities phased at the ephemerides of TOI-942b and TOI-942c, with the corresponding 3σ upper limit for each planet marked by the dashed curve. Note that while the velocities of TOI-942b appear to phase well with its transit ephemeris, this should be attributed to the stellar activity signal being at a similar timescale to the orbital period.

speckle auto-correlation functions (ACFs) from these observations are shown in Figure 11. No stellar companions were detected for either target star.

We also obtained speckle observations of TOI-942 with Alopeke at the 8 m Gemini-North observatory, located on Maunakea, Hawaii. The observation, obtained on 2019 October 14, incorporates a 1 minute integration involving 1000 60 ms exposures of 256×256 pixel subarrays about the target star. These observations have resulting spatial resolutions of 0.016 FWHM in the blue and $0''.025$ in the red, yielding an inner working angle of ~ 3 au at the distance to TOI-942. The analysis and detection limits were derived per Howell et al. (2011, 2016). The speckle images and limits on companions are shown in Figure 12. Note that the observations were

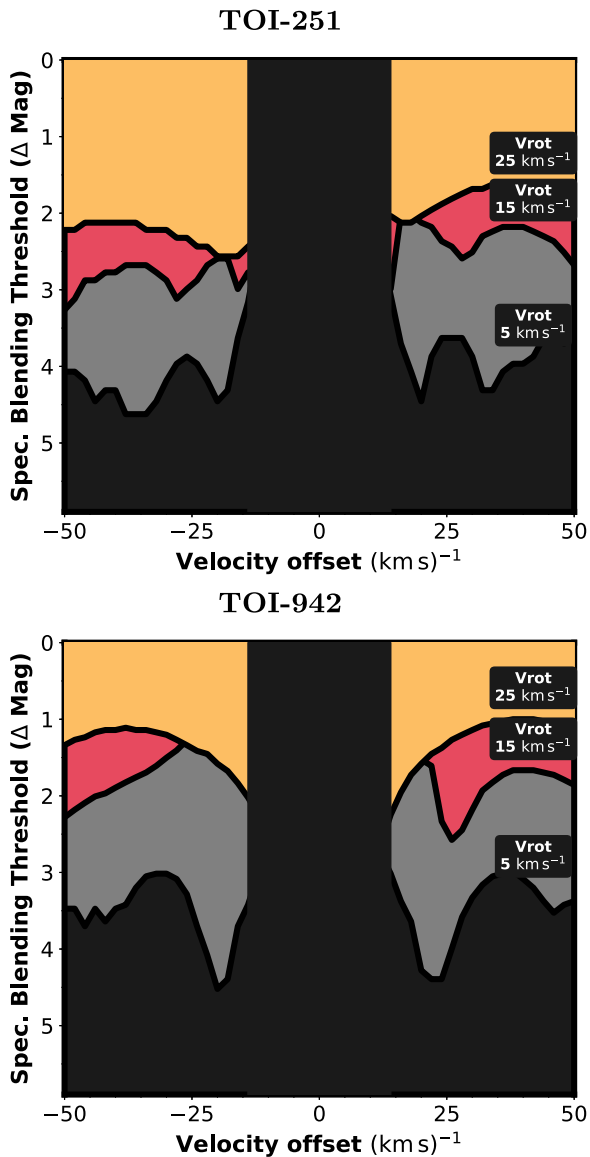


Figure 8. Detection threshold for any blended spectroscopic companions to the target stars via CHIRON observations. Colored regions show the excluded parameter space for any blended stars as a function of their magnitude difference to the target star Δmag and their velocity separation. Our ability to detect such companions depends on their rotational line broadening. The simulation shows the detection thresholds for a blended star of $v_{\text{rot}} = 5, 15,$ and 25 km s^{-1} , with the detectability progressively worsening for more rapidly rotating companions. The black regions show where no companions can be detected. For low-velocity separations, there is a degeneracy between any blended companion and the target star, and as such, we are not sensitive to such scenarios. As the broadening profiles have structured noise features, some velocities are systematically more sensitive to secondary companions than other regions.

obtained at relatively high airmass, and as such, the blue reconstructed image is adversely affected. No stellar companions are detected in either channel.

3. Elimination of False-positive Scenarios

A number of astrophysical false-positive scenarios can imitate the transit signals of planetary systems. Eclipsing binaries in grazing geometries or nearby faint eclipsing binaries can exhibit transits of depths similar to that of transiting super-Earths and Neptunes in extreme scenarios.

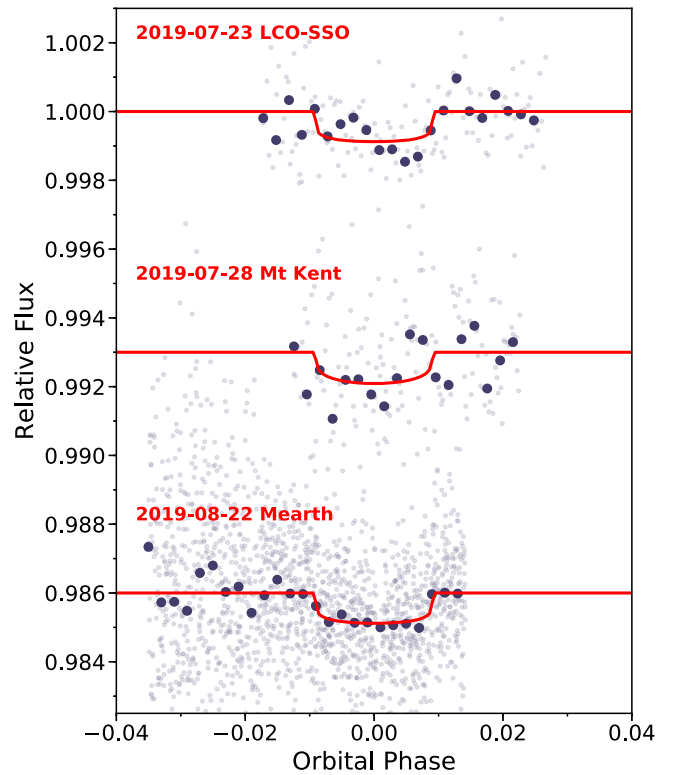


Figure 9. Ground-based follow-up light curves of TOI-251b. The light curves from each facility are shown with an arbitrary vertical offset applied. The filled points mark the binned fluxes at phase intervals of 0.002. The observatory, date, and filter of each observation are labeled. Observations by the MEarth observatory were taken in the MEarth band.

The possibility that our target stars are actually grazing eclipsing binaries is extremely unlikely given their well-resolved box-shaped transits. Nevertheless, we obtained a series of radial velocity observations for both target stars. Radial velocity variation at the $>1 \text{ km s}^{-1}$ level can be indicative of the companion being of stellar mass or the target star being spectroscopically blended with a background eclipsing binary.

We obtained nine spectra of each target star and derived radial velocities from each via a least-squares deconvolution analysis (Section 2.2.1). As expected for young stars, these velocities exhibited significant astrophysical jitter beyond their velocity uncertainties. The mean uncertainty of the velocities for TOI-251 is 17 m s^{-1} , while the velocity scatter is significantly higher at 73 m s^{-1} . Similarly, the mean uncertainty in the velocities of TOI-942 is 35 m s^{-1} , but the velocity scatter is at 127 m s^{-1} .

Nevertheless, the lack of a detectable radial velocity orbit to within 1 km s^{-1} for both target stars rules out the possibility that they are orbited by stellar companions. In Section 5, we derive upper limits to the masses of any orbiting companions around our target stars. The velocities of each system are modeled assuming circular orbits for each planet; the stellar activity is accounted for via a jitter term. We make no attempts at correcting for the stellar jitter via decorrelation against stellar activity indicators, and we do not make use of Gaussian processes to model possible rotational signals in the velocities. Through this simple exercise, we find 3σ mass upper limits of $<1.0 M_{\text{Jup}}$ for TOI-251b, $<2.6 M_{\text{Jup}}$ for TOI-942b, and

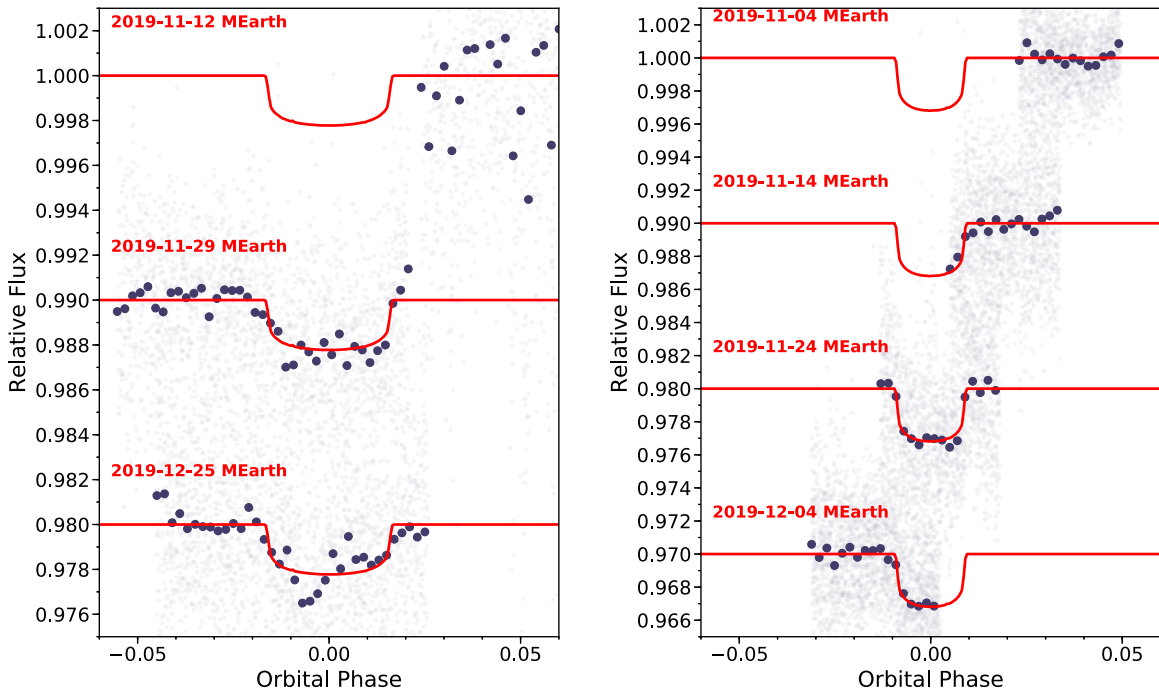


Figure 10. Ground-based follow-up light curve of TOI-942b (left) and TOI-942c (right). The light curves were gathered by the MEarth observatory.

Table 3
Summary of Photometric Observations

Target	Facility	Date(s)	Number of Images ^a	Cadence (s) ^b	Filter
TOI-251	WASP	2006-05-15 to 2014-12-06 (over 8 observing campaigns)	132,002	37	WASP
TOI-251	TESS	2018-08-23 to 2018-09-20	18,316	120	TESS
TOI-251	LCO-SSO	2019-07-23	148	127	Y
TOI-251	MKO	2019-07-28	168	89	i'
TOI-251	MEarth	2019-08-22	1749	12	MEarth band
TOI-942	WASP	2006-09-15 to 2014-12-09 (over 10 observing campaigns)	87,361	30	WASP
TOI-942	TESS	2018-11-15–2018-12-11	1188	1799	TESS
TOI-942	MEarth	2019-11-05	1680	10	MEarth band
TOI-942	MEarth	2019-11-13	1791	10	MEarth band
TOI-942	MEarth	2019-11-15	1814	11	MEarth band
TOI-942	MEarth	2019-11-17	2346	6	MEarth band
TOI-942	MEarth	2019-11-25	1974	10	MEarth band
TOI-942	MEarth	2019-11-30	2049	11	MEarth band
TOI-942	MEarth	2019-12-05	2488	10	MEarth band
TOI-942	MEarth	2019-12-26	2223	5	MEarth band

Notes.

^a Outlying exposures have been discarded.

^b Median time difference between points in the light curve. Uniform sampling was not possible due to visibility, weather, and pauses.

$< 2.5 M_{\text{Jup}}$ for TOI-942c. Future examination making use of stellar activity markers can further refine the masses of these planets.

The $22'' \text{ pixel}^{-1}$ plate scale of TESS often makes it difficult to distinguish the true source of transit signals in crowded fields. Fainter eclipsing binaries whose depths are diluted by the flux from the target star can often be misinterpreted as planet candidates. We obtained ground-based follow-up photometric confirmation of all planet candidates around TOI-251 (Figure 9) and TOI-942 (Figure 10). The on-target detection of the transits shows that the transit signal originates from the target stars to within the spatial resolution of $\sim 1''$ of our ground-based follow-up facilities.

From the high spatial resolution speckle images presented in Section 2.4, we can also eliminate the presence of any stellar companions with $\Delta M < 4$ within $\sim 0''.2$ of our target stars. No Gaia stars are cataloged within $2''$ of these target stars. Similarly, no slowly rotating spectroscopic blended companions were detected from our CHIRON observations (Section 2.2.1) at $\Delta M < 4$.

We can estimate the probability that a faint eclipsing binary lying unresolved by our high-resolution speckle images is causing the transit signals. The transit shape and the ratio between the ingress and totality timescales can inform us about the brightness of any diluted background eclipsing binary that may be causing the transit signal (Seager & Mallén-Ornelas 2003). We follow

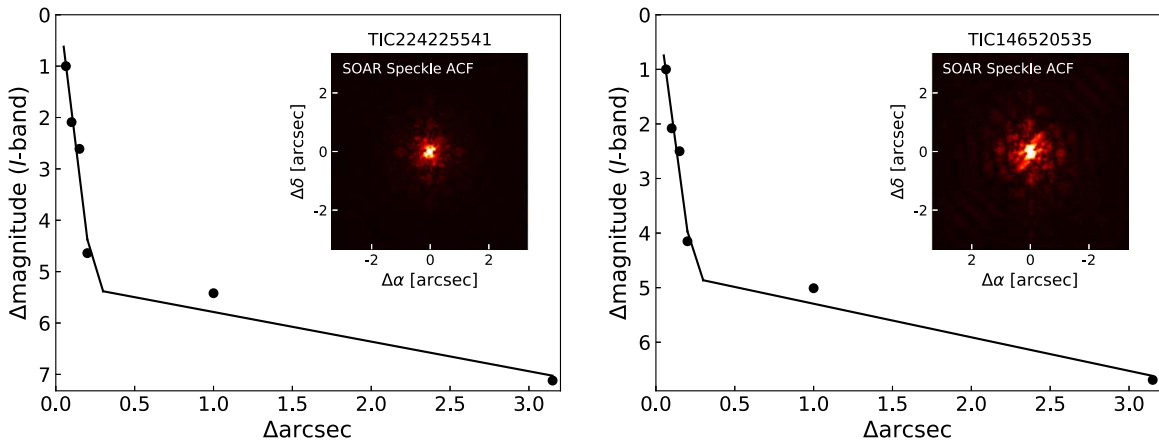


Figure 11. SOAR speckle observations of TOI-251 (left) and TOI-942 (right). The 5σ detection sensitivity to companions is shown in each figure. The insets show the ACFs for each observation. No stellar companions were detected near either target star.

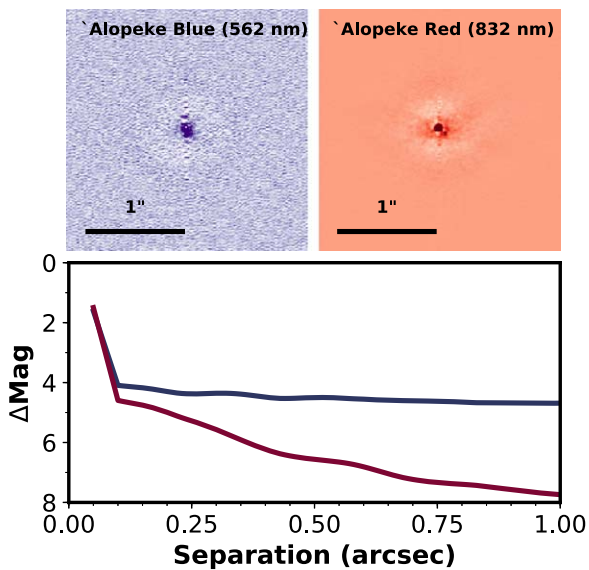


Figure 12. Gemini-North Alopeke speckle images of TOI-942 in the blue (top left) and red (top right) channels. Bottom panel: corresponding limiting magnitudes for companions as a function of angular distance to the target star.

Vanderburg et al. (2019) and estimate the brightest possible background eclipsing binary that may be inducing our transit signal. The maximum difference in magnitude is given by $\Delta m_{\text{TESS}} \leq 2.5 \log_{10}(T_{12}^2/T_{13}^2 \delta)$, where T_{12} is the duration of ingress, T_{13} is the duration between first and third contact, and δ is the depth of the transit.

We find that for TOI-251b, the transit can only be caused by a background eclipsing binary with $\Delta m_{\text{TESS}} \leq 3.40$ and 3.0σ significance. From our diffraction-limited observations of TOI-251, we excluded stellar blends within $0''.2$ to a brightness contrast of ≈ 3 mag. For a randomly chosen star in a direction near TOI-251, the density of $2.0 \leq \Delta m_{\text{TESS}} \leq 3.4$ stars within the ground-based exclusion radius of $0''.2$ is $< 3 \times 10^{-5}$. Though TOI-251 is not randomly chosen, it is far from the galactic plane, where background eclipsing binaries are expected to be roughly 2 orders of magnitude less common than true planets (Sullivan et al. 2015, Figure 30). While not formally impossible, the combined transit shape, lack of companions detectable by diffraction-limited imaging, lack of secondary spectroscopic lines, and line of sight of TOI-251

lead background eclipsing binary scenarios to be highly disfavored.

For TOI-942, a similar calculation yields that a background eclipsing binary no fainter than 2.68 mag is required to cause the transits of either one of its two planets. If it were a randomly chosen star, then the chance of there being another background star within $0''.2$ is $< 6 \times 10^{-5}$ at $\Delta m_{\text{TESS}} < 2.68$. The chance that two such background eclipsing binaries exist, inducing our multiplanet transiting signal, is $< 4 \times 10^{-9}$. The low probability of such an occurrence, the multiplanet nature of the system, and the lack of any companions from diffraction-limited imaging and spectroscopy lead to eclipsing binary scenarios being disfavored.

4. Estimating the Age of Young Field Stars

It is notoriously difficult to estimate the ages of field stars. However, young Sun-like stars exhibit rotational and activity-induced photometric and spectroscopic behavior that makes it possible to approximate their ages. These activity and rotation period properties can typically be calibrated via well-characterized clusters (Mamajek & Hillenbrand 2008) to provide age relationships that can be used for dating purposes.

Sun-like stars spin down over their main-sequence lifetimes through mass loss via stellar-wind processes. While the Sun has a present-day rotation period of 24 days, similar stars in the 120 Myr old Pleiades cluster have rotation periods of ~ 4 days. The rapid rotation and consequentially stronger dynamo of young stars excite strong spot and chromospheric activity. Observable chromospheric activity indicators, such as emission in the core of the Ca II lines, as well as X-ray emission, can be used as proxies for the rotation and age of young Sun-like stars. The element lithium is destroyed in the cores of Sun-like stars through proton collisions. Through convective mixing processes, this leads to a rapid depletion of lithium in the stellar atmosphere within the first ~ 500 Myr of their lives. The strength of the lithium 6708 Å absorption feature has traditionally been used as a youth indicator for Sun-like stars.

We made use of these photometric and spectroscopic properties to estimate the ages of TOI-251 and TOI-942. Though these estimates are imprecise given the field nature of our target stars, they generally agree sufficiently for us to place meaningful age constraints on these target stars.

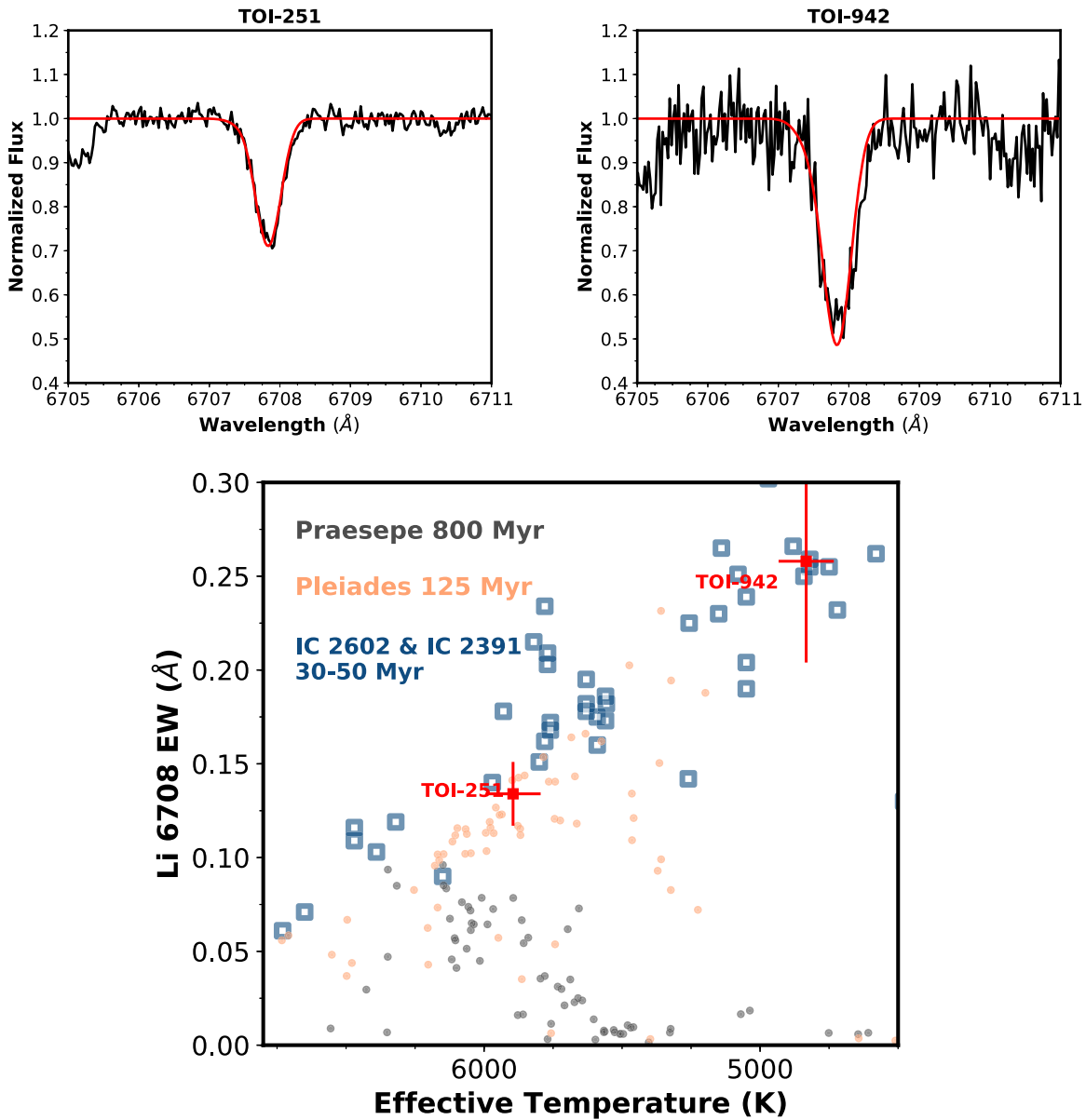


Figure 13. Both TOI-251 and TOI-942 exhibit strong lithium absorption at 6708 Å. We fit this absorption feature with a Gaussian doublet at 6707.76 and 6707.91 Å and a single Fe I line at 6707.43 Å. The absorption features and best-fit models of TOI-251 are shown in the top left panel, and TOI-942 is shown in the top right panel. The bottom panel compares the equivalent widths of the lithium feature against stars in the IC 2602, IC 2391, Pleiades, and Praesepe clusters and associations. Measurements for Pleiades and Praesepe were obtained as part of this work using the methodology described above. Measurements for IC 2602 and IC 2391 are adopted from Randich et al. (1997) and Randich et al. (2001).

4.1. Lithium Depletion

The strength of atmospheric lithium absorption in the spectra of convective envelope stars is also a commonly adopted age indicator. We make use of the Li 6708 Å line as another age estimator for our targets. The Li line equivalent widths are estimated by fitting three Gaussian profiles, accounting for the Li doublet at 6707.76 and 6707.91 Å and the nearby Fe I line at 6707.43 Å that is often blended with the Li features. Each line is assumed to be of equal width, and the two Li lines are also assumed to be of equal height. Using the TRES observations we obtained for both target stars, we measured the equivalent widths of the Li 6708 Å line to be 0.134 ± 0.017 Å for TOI-251 and 0.257 ± 0.054 Å for TOI-942.

To compare the lithium absorption feature of our target stars against stars in well-characterized clusters and associations, we

obtained a series of spectra of members of the IC 2602, IC 2391, Pleiades, and Praesepe groups. Spectra and measurements of Pleiades and Praesepe members come from long-term radial velocity surveys for planets in open clusters using the TRES spectrograph. Two such surveys, in Praesepe and the Hyades, are described in Quinn et al. (2012, 2014). With the goal of measuring low-amplitude radial velocity variation, the spectra have a typically high signal-to-noise ratio and therefore support precise measurement of Li equivalent widths. The Li measurements for IC 2602 and IC 2391 members are adapted from Randich et al. (1997, 2001).

Figure 13 shows the Li 6708 Å equivalent widths of the target stars in comparison with the same measurements for membership stars. The Li line strength of TOI-251 agrees with that of Pleiades members, while TOI-942 exhibits significantly stronger Li absorption than equivalent stars in Pleiades.

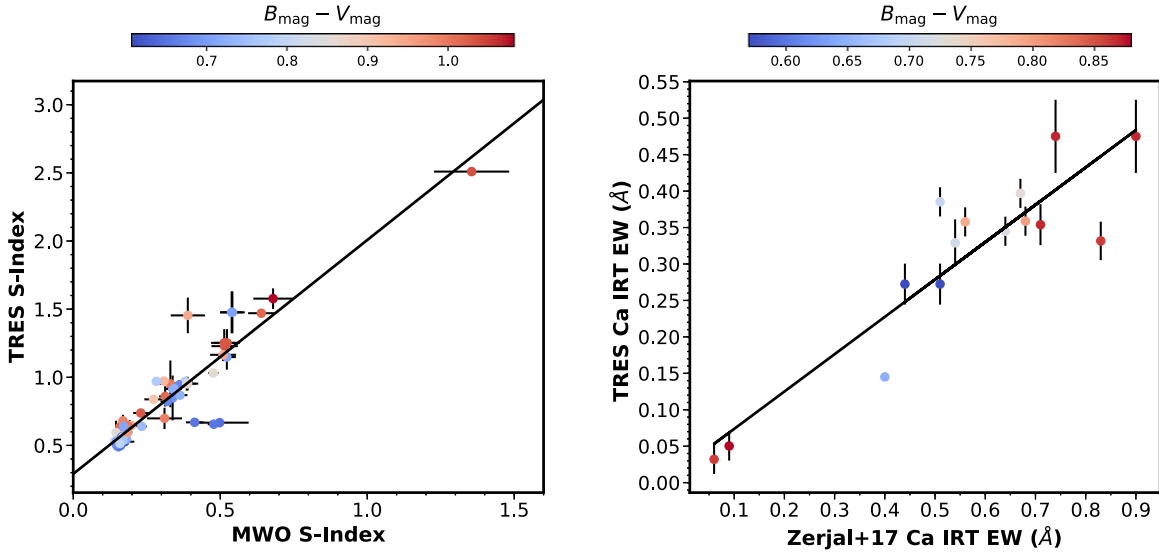


Figure 14. Calibrations for our measurements of the Ca II HK and infrared triplet activity indices. The left panel shows the S_{HK} index of Mount Wilson stars as measured by TRES observations. We find an agreement between our measurements and those from the literature to within $\Delta S_{HK} = 0.078$. The right panel shows the equivalent width measurements of the Ca II infrared triplet core emission for stars that have both archival TRES observations and were surveyed in Žerjal et al. (2017). We find that a linear transformation is also sufficient to transform our measured values from TRES to those reported in the literature, with a resulting scatter in the equivalent widths of $\Delta EW_{IRT} = 0.053 \text{ \AA}$.

4.2. Activity–Age Relationships

Both stars exhibit significant chromospheric emission in the near-ultraviolet (NUV) Ca II H and K lines and the near-infrared Ca II triplet. Both stars are also detected in the X-ray with the ROSAT all-sky survey, while TOI-942 is detected in the GALEX NUV band. Chromospheric emission is a proxy for stellar rotation, being generated due to the stronger magnetic dynamo of the rapidly rotating young stars (e.g., Noyes et al. 1984). We make use of the Mount Wilson S_{HK} index to compare the chromospheric emission of our target stars from the TRES spectra against literature activity–age relationships, as explained in the next section.

4.2.1. Ca II HK Emission

Both Ca II H (3969 Å) and K (3934) lines are captured within TRES echelle orders. We measure Ca II HK emission core emissions in a band 1 Å wide centered about each line. The baseline flux is estimated from 5 Å wide bands over the continuum regions on either side of the line center. Figure 14 shows our calcium line strength measurements for Sun-like stars ($5000 \text{ K} < T_{\text{eff}} < 6000 \text{ K}$) against that of catalog S_{HK} values of the same stars from the Mount Wilson Observatory HK Project (Vaughan et al. 1978; Wilson 1978; Duncan et al. 1991; Baliunas et al. 1995). With the exception of a few active outlying stars, we find that our line emission flux estimates can be translated to the S_{HK} index with a simple linear transformation with an uncertainty of $\Delta S_{HK} = 0.078$. The Ca II HK line strength, as a function of the bolometric flux (R'_{HK}), is then calibrated using the relationship from Noyes et al. (1984) via the *PyAstronomy* (Czesla et al. 2019) *SMW_RHK* function. The S_{HK} and R'_{HK} values for the target stars are listed in Table 4. The uncertainties in these values are computed as the quadrature addition of uncertainty in the TRES emission flux to S_{HK} calibration and the scatter of the measurements between each observation.

The Ca II HK luminosity can be correlated with stellar age. We make use of the calibration from Mamajek & Hillenbrand (2008; Equation (3)) to calculate the Ca II HK ages of our target stars.

Consistent with the gyrochronology estimate, TOI-251 has an age of 27^{+21}_{-13} Myr, with a 3σ regime ranging from 3 to 170 Myr. It is estimated that TOI-942 has an age of 10^{+12}_{-6} Myr, with a 3σ upper limit of 100 Myr. The activity age estimate is significantly younger than that from gyrochronology. We note that with $\log R'_{HK} = -4.019 \pm 0.064$, the Ca II HK emission from TOI-942 is near the limits of the calibrated range of the Mamajek & Hillenbrand (2008) relations of $-5.0 < \log R'_{HK} < -4.0$, corresponding to a lower age boundary of 8 Myr. Stars as young as TOI-942 have saturated chromospheric emission features, making it difficult for us to derive precise ages from these spectroscopic indicators.

4.2.2. Infrared Ca II Triplet Emission

The infrared Ca II triplet at 8498, 8542, and 8662 Å also exhibits line core emission in active stars. Both TOI-251 and TOI-942 exhibit strong core emission in the infrared. The 8498 and 8542 Å lines are well placed within the TRES spectral orders. To measure the core emission equivalent widths of these lines, we first fit and remove a synthetic spectral template and fit the residuals about the calcium lines with a Gaussian profile. The synthetic template is an ATLAS9 (Castelli & Kurucz 2004) atmosphere model, convolved with the instrumental and rotational broadening kernel of the target star. The synthetic template is then subtracted from the continuum-normalized observed spectrum. The resulting residuals about each calcium line are fitted with a Gaussian with width corresponding to the line broadening of the spectrum and with centroid fixed to the expected central wavelength of each line.

Figure 14 shows the equivalent widths as measured from TRES against the same stars that were characterized by Žerjal et al. (2017). For Sun-like stars, a linear transformation between our TRES observations and the literature values is sufficient, with a scatter in the resulting relationship of $\Delta EW_{IRT} = 0.053 \text{ \AA}$.

We measure Ca II infrared triplet equivalent widths of $EW_{IRT} = 0.61 \pm 0.10 \text{ \AA}$ for TOI-251 and $1.73 \pm 0.17 \text{ \AA}$ for TOI-942. Žerjal et al. (2017) offered a qualitative age–calcium

Table 4
Stellar Parameters

Parameter	TOI-251	TOI-942	Source
Catalog Information			
TIC	224225541	146520535	Stassun et al. (2018)
Tycho-2	7520-00369-1	5909-00319-1	Høg et al. (2000)
Gaia DR2 source ID	6539037542941988736	2974906868489280768	Gaia Collaboration et al. (2018b)
Gaia R.A. (2015.5)	23:32:14.9	05:06:35.91	Gaia Collaboration et al. (2018b)
Gaia decl. (2015.5)	−37:15:21.11	−20:14:44.21	Gaia Collaboration et al. (2018b)
Gaia μ_α (mas yr ^{−1})	44.639 ± 0.074	15.382 ± 0.034	Gaia Collaboration et al. (2018b)
Gaia μ_δ (mas yr ^{−1})	1.902 ± 0.070	−3.976 ± 0.040	Gaia Collaboration et al. (2018b)
Gaia DR2 parallax (mas)	10.019 ± 0.044	6.524 ± 0.029	Gaia Collaboration et al. (2018b)
Systemic radial velocity (km s ^{−1}) ^a	−2.059 ^{+0.026} _{−0.030}	25.321 ^{+0.034} _{−0.032}	...
<i>U</i> (km s ^{−1})	−19.454 ± 0.085	−15.729 ± 0.030	
<i>V</i> (km s ^{−1})	−7.190 ± 0.045	−22.347 ± 0.045	
<i>W</i> (km s ^{−1})	−4.550 ± 0.039	−5.252 ± 0.040	
Stellar Atmospheric Properties			
<i>T</i> _{eff,*} (K)	5875 ⁺¹⁰⁰ _{−190}	4928 ⁺¹²⁵ _{−85}	
[Fe/H] ^a	−0.106 ^{+0.079} _{−0.070}	−0.221 ^{+0.131} _{−0.076}	
<i>v</i> sin <i>I</i> _* (km s ^{−1})	11.5 ± 1.0	14.3 ± 0.5	
<i>v</i> _{macro} (km s ^{−1})	7.9 ± 1.0	9.8 ± 3.4	
Stellar Activity Properties			
<i>P</i> _{rot} (days)	3.84 ± 0.48	3.40 ± 0.37	
<i>S</i> _{HK} (Å)	0.616 ± 0.083	1.06 ± 0.15	
log <i>R</i> ' _{HK}	−4.119 ± 0.066	−4.019 ± 0.064	
Ca II IRT EW (Å)	0.61 ± 0.10	1.73 ± 0.17	
ROSAT X-ray counts (CTS)	0.01477	0.0446 ± 0.0130	Rosat (2000); Voges et al. (2000)
ROSAT X-ray hardness ratio HR ₁	−0.39 ± 0.12	0.17 ± 0.28	Rosat (2000); Voges et al. (2000)
X-ray luminosity log <i>L</i> _x / <i>L</i> _{bol}	−4.45 ± 0.36	−3.12 ± 0.16	
Li 6708 EW (Å)	0.134 ± 0.017	0.257 ± 0.054	
Photometric Properties			
GALEX NUV (mag)		18.507 ± 0.049	Bianchi et al. (2017)
TESS <i>T</i> (mag)	9.3258 ± 0.0061	11.0462 ± 0.0066	Stassun et al. (2018)
Gaia <i>G</i> (mag)	9.7541 ± 0.0012	11.6346 ± 0.0014	Gaia Collaboration et al. (2018b)
Gaia <i>B</i> _p (mag)	10.1070 ± 0.0030	12.1468 ± 0.0034	Gaia Collaboration et al. (2018b)
Gaia <i>R</i> _p (mag)	9.2910 ± 0.0026	10.9950 ± 0.0029	Gaia Collaboration et al. (2018b)
TYCHO <i>B</i> (mag)	10.528 ± 0.068	12.783 ± 0.364	Perryman et al. (1997)
TYCHO <i>V</i> (mag)	9.8870 ± 0.0050	11.982 ± 0.026	Perryman et al. (1997)
2MASS <i>J</i> (mag)	8.766 ± 0.020	10.231 ± 0.022	Skrutskie et al. (2006)
2MASS <i>H</i> (mag)	8.498 ± 0.044	9.747 ± 0.023	Skrutskie et al. (2006)
2MASS <i>K</i> _s (mag)	8.426 ± 0.027	9.639 ± 0.023	Skrutskie et al. (2006)
WISE <i>W</i> ₁ (mag)	8.372 ± 0.024	9.576 ± 0.024	Wright et al. (2010); Cutri et al. (2014)
WISE <i>W</i> ₂ (mag)	8.399 ± 0.020	9.609 ± 0.020	Wright et al. (2010); Cutri et al. (2014)
WISE <i>W</i> ₃ (mag)	8.368 ± 0.022	9.453 ± 0.039	Wright et al. (2010); Cutri et al. (2014)
Stellar Properties			
<i>M</i> _* (<i>M</i> _⊙)	1.036 ^{+0.013} _{−0.009}	0.788 ^{+0.037} _{−0.031}	
<i>R</i> _* (<i>R</i> _⊙)	0.881 ^{+0.038} _{−0.047}	1.022 ^{+0.018} _{−0.020}	
log <i>g</i> _* (cgs)	4.560 ^{+0.046} _{−0.046}	4.314 ^{+0.028} _{−0.028}	
<i>L</i> _* (<i>L</i> _⊙)	0.831 ^{+0.105} _{−0.072}	0.428 ^{+0.166} _{−0.079}	
Line-of-sight inclination <i>I</i> _* (deg)	78 ⁺⁷ _{−14} (>43 3σ)	76 ⁺⁹ _{−11} (>45 3σ)	
Age (Myr)	40–320	20–160	
Distance (pc)	99.52 ^{+0.44} _{−0.43}	152.76 ^{+0.71} _{−0.71}	

Note.^a Derived from the global modeling described in Section 5, co-constrained by spectroscopic stellar parameters and the Gaia DR2 parallax.

triplet relationship from their calibration of cluster stars. The infrared triplet emission of TOI-251 makes it compatible with similar stars in the 100–1000 Myr range, while TOI-942 falls in the <100 Myr age range.

4.2.3. X-Ray Emission

Young, rapidly rotating stars are also known to exhibit X-ray emission. The star TOI-251 is an X-ray source in the Second

ROSAT Source Catalog of Pointed Observations (Rosat 2000), while TOI-942 is an X-ray source in the ROSAT All-Sky Faint Source Catalog (Voges et al. 2000). Their X-ray count rates, hardness ratios, and luminosities are provide in Table 4. We adopt the calibration provided in Fleming et al. (1995) for the conversion from the X-ray count rate (CTS) to an X-ray luminosity (*L*_x), finding an X-ray luminosity of log(*L*_x/*L*_{bol}) = −4.45 ± 0.36 for TOI-251 and −3.12 ± 0.16 for TOI-942. Using the age–X-ray luminosity relationship from Mamajek &

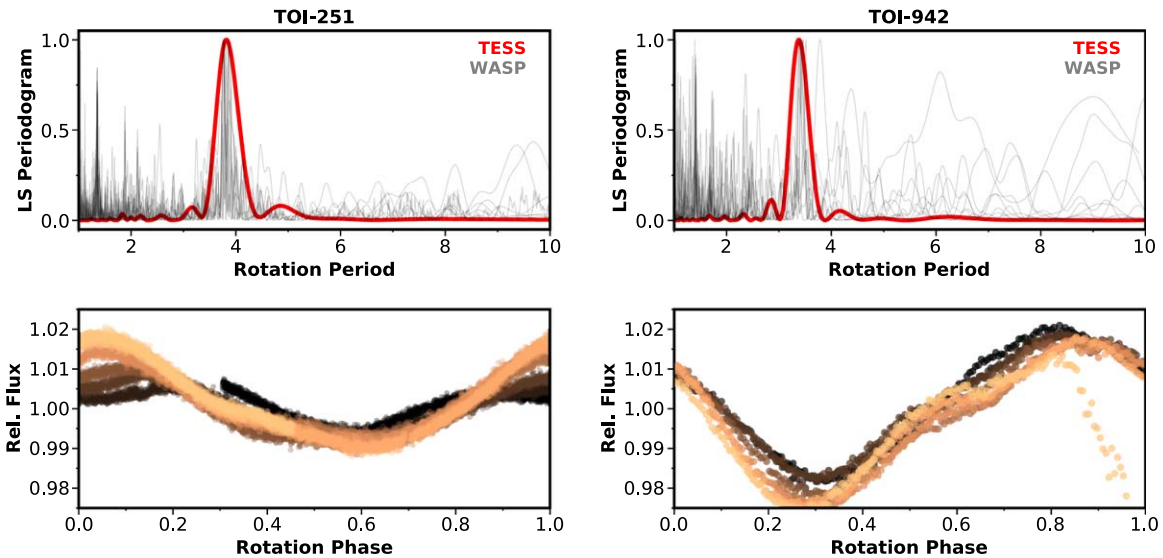


Figure 15. Both TOI-251 and TOI-942 show significant spot modulation in their light curves. The top panels show the Lomb–Scargle periodogram of the TESS light curves (red) and each campaign of the WASP observations (gray). The rotation period is consistently detected in the single sector of TESS observations and the 8 yr of monitoring from WASP. The bottom panels show the TESS light curve folded to the rotation period. Each rotation period is overplotted with a slightly different color gradient, such that it is easier to discern the spot variations over the course of the TESS observations.

Hillenbrand (2008; Equation (A3)), we derive an estimated age of 280_{-180}^{+550} Myr for TOI-251, but the 3σ age upper limit is not constraining due to the scatter in the distribution. For TOI-942, we find an X-ray age of 7_{-4}^{+11} Myr, with a 3σ upper limit of 250 Myr. Like our Ca II HK and infrared triplet estimates, the X-ray luminosity is saturated for this calibration above $\log(L_x/L_{\text{bol}}) = 4.0$ (corresponding to an 8 Myr lower limit). The star TOI-942 is more active than the calibrated range of the Mamajek & Hillenbrand (2008) relationships, so our age estimate is at best qualitative.

4.2.4. NUV Detection

Ultraviolet emission from active chromospheres can also be an indicator of youth for Sun-like stars. The star TOI-942 has a measurable flux in the NUV band of the GALEX all-sky catalog (Bianchi et al. 2017). Findeisen et al. (2011) calibrated an $\text{NUV} - J/J - K$ color–color relationship using Hyades, Blanco 1, and moving group members, with a resulting scatter in the determined log ages of 0.39 dex. We adopt this relationship and find an NUV age for TOI-942 of 60_{-40}^{+130} Myr. We note that there is significant scatter in the relationship between NUV flux and age, and as such, the 3σ range of the NUV age estimate is only constraining to <1 Gyr.

4.3. Rotation Period and Gyrochronology

Both TOI-251 and TOI-942 exhibit significant spot-induced rotational modulation in their TESS light curves. These light curves, folded over the rotational period, are shown in Figure 15. The periodograms from a Lomb–Scargle analysis of the single sector of TESS observations, as well as each observing campaign of the WASP observations, are shown.

From the TESS light curves, we measure a rotation period for TOI-251 of 3.84 ± 0.48 days, while TOI-942 has a rotation period of 3.40 ± 0.37 days. Similarly, the WASP observations yielded rotation periods of 3.799 ± 0.047 days for TOI-251 and 3.41 ± 0.49 for TOI-942. The longevity of this activity

signal from TESS and WASP gives us confidence that the periodicity we quote is the rotation period of the host stars.

We adopt a few gyrochronology relationships to estimate the ages of TOI-251 and TOI-942. These relationships were calibrated by interpolating the slow-rotating sequence in well-characterized clusters. We note that by adopting these relationships, we are making the assumption that TOI-251 and TOI-942 follow the age spin-down trends seen in slow rotators among Sun-like stars. Many of these young clusters also show a spread in rotation at a given mass. By Pleiades age, the rapid rotators are usually all binaries (e.g., Douglas et al. 2016; Stauffer et al. 2018), but at the youngest ages, we cannot confirm that our stars lie on the main sequence. If TOI-251 and TOI-942 are rapid rotators for their age, then their ages will be difficult to estimate using gyrochronology. Given that both stars exhibit significant chromospheric activity and lithium absorption, we think it is reasonable to assume that these stars are relatively young. By assuming that they are also slow rotators for their age, we can apply gyrochronology relations to derive an additional age constraint.

Using the relationship in Barnes (2007), we find an age T_{gyro} of 110_{-60}^{+30} Myr for TOI-251, with a 3σ age range of 40–220 Myr. At 50 ± 13 Myr, TOI-942 is considerably younger, with a 3σ age range of 20–90 Myr. The uncertainties are the quadrature addition of the intrinsic uncertainties in the gyrochronology relationship as prescribed in Barnes (2007) and the uncertainties resulting from the TESS rotation period measurements. Similarly, applying the age relationship from Mamajek & Hillenbrand (2008), we get an age range of 70–318 Myr for TOI-251 and 41–155 Myr for TOI-942.

Qualitatively, we can compare the rotation periods of our target stars against those in known clusters and associations. Figure 16 shows the rotation periods of the target stars against known members of the 120 Myr old Pleiades measured by Rebull et al. (2016) and 800 Myr old Praesepe measured by Rebull et al. (2017). For comparison, we also plot the rotation of members of the *h* Persei cluster at an age of 13 Myr from Moraux et al. (2013) to illustrate that both TOI-251 and TOI-942 are older than some of the youngest clusters and

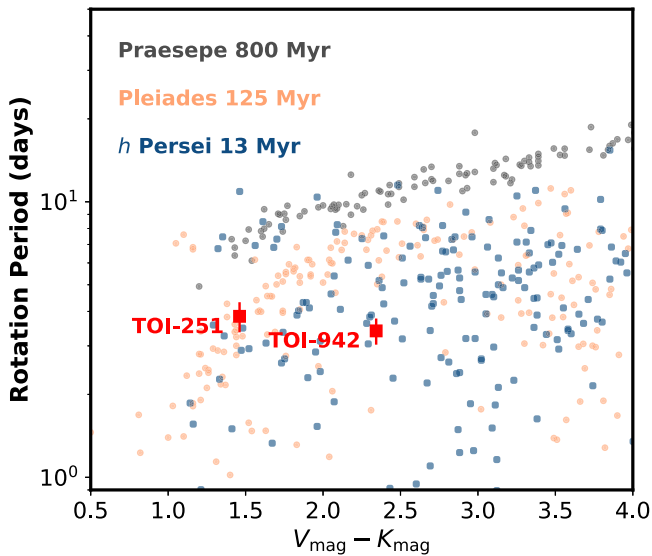


Figure 16. Comparison between the rotation periods of TOI-251 and TOI-942 against stars from known clusters and associations. The blue squares mark stars from the 13 Myr old *h* Persei cluster as measured by Moraux et al. (2013), with colors dereddened from 3D dust maps. The orange points show the distribution of rotation periods for stars in the 125 Myr Pleiades cluster from Rebull et al. (2016). The gray points show stars in the \sim 800 Myr Praesepe cluster measured by Rebull et al. (2017). While TOI-251 has rotation periods similar to stars from the Pleiades, TOI-942 appears younger than the majority of single stars from the Pleiades but older than Sun-like stars near the zero-age main sequence in the *h* Persei cluster.

associations. The *h* Persei members are marked by the blue squares in Figure 16. The colors of the stars in *h* Persei have been dereddened according to the 3D dust maps via *dustmap* (Green 2018) using maps from Green et al. (2019). In this qualitative comparison, the rotation period of TOI-251 agrees well with the Pleiades population, supporting the gyrochronology estimate of \sim 110 Myr. The star TOI-942 is rotating faster than an equivalent star within the Pleiades distribution, and as such supports our estimate of it being younger than 100 Myr. We note, though, that there is a possibility for our targets to be young, rapid rotators, as with stars in the significantly younger *h* Persei cluster.

4.3.1. Infrared Excess

The spectroscopic and gyrochronology age estimates described above have placed meaningful upper age limits. Lower limits from these measurements are more difficult for TOI-942 given that many of its activity indicators are saturated.

A qualitative argument for the lower limits of both TOI-251 and TOI-942 can be made due to their lack of any infrared excess in the WISE bands. The spectral energy distributions (SEDs) of TOI-251 and TOI-942 are shown in Figure 19. Disks can be traced by $H\alpha$ emission and infrared excess and typically dissipate by \sim 5–10 Myr (see reviews by Mamajek 2009; Williams & Cieza 2011). As such, we adopt a lower limit of 10 Myr for the age of TOI-942.

4.3.2. Color–Magnitude Diagram

Further lower-bound age limits may be inferred by comparing the colors and magnitudes of the target stars against members of well-known clusters. Figure 17 shows the Gaia color–magnitude diagram for TOI-251 and TOI-942. Stars

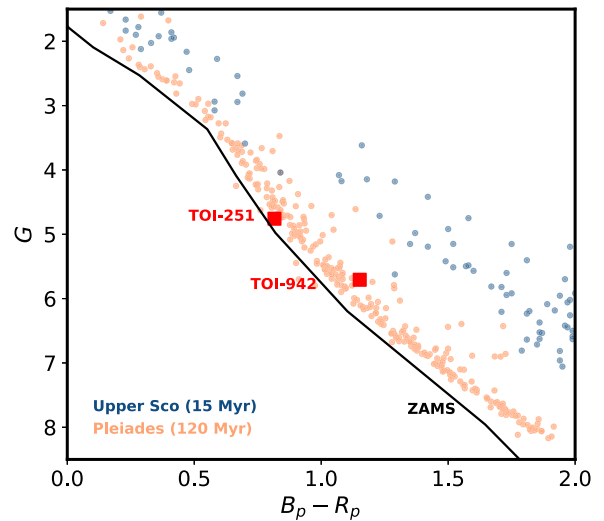


Figure 17. Gaia color–magnitude diagram of TOI-251 and TOI-942. For comparison, stars from the 120 Myr old Pleiades cluster (Lodieu et al. 2019) and the 15 Myr old Upper Sco association are shown (Damiani et al. 2019). While TOI-251 lies close to the distribution of stars in the Pleiades cluster, TOI-942 lies marginally above the stars in the Pleiades but is clearly older than the pre-main-sequence stars in Upper Sco. For reference, the zero-age main sequence from the MIST isochrones is marked by the black line (Dotter 2016).

from the 120 Myr old Pleiades cluster (Lodieu et al. 2019) and 15 Myr old Upper Sco association (Damiani et al. 2019) are shown for comparison.

The star TOI-251 is consistent with having an age similar to stars in the Pleiades cluster, based on our spectroscopic and gyrochronology estimates above. Having reached the main sequence, it is difficult to estimate its age from the SED, and the ages from isochrone models provide no further constraints to the age of the system.

The star TOI-942 lies marginally above the zero-age main sequence. The activity-based age estimates described above have trouble placing a lower bound on the age of TOI-942. From the color–magnitude diagram, TOI-942 clearly sits below stars from the 15 Myr old Upper Sco association. As part of the global analysis, the isochrone-fitted age from Section 5 provides a 3σ lower age limit of 23 Myr, consistent with that provided by gyrochronology.

4.4. Kinematics

To the best of our knowledge, neither TOI-251 nor TOI-942 is a member of any known coeval stellar population. To check, we searched the CDIPS target star list (Bouma et al. 2019 Table 1), which is a concatenation of stars from across the literature reported to be in known moving groups and open clusters. This concatenation included large surveys ($>10^5$ cluster stars) such as those of Kharchenko et al. (2013), Dias et al. (2014), Oh et al. (2017), Cantat-Gaudin et al. (2018, 2019), Gaia Collaboration et al. (2018a), Zari et al. (2018), and Kounkel & Covey (2019). It also included targeted surveys, for instance, those of Bell et al. (2017), Gagné et al. (2018a, 2018b), and Gagné & Faherty (2018), Kraus et al. (2014), Röser et al. (2011), Rizzuto et al. (2011). We also verified that we could not place these targets into any known associations via the online BANYAN Σ tool (Gagné et al. 2018a).

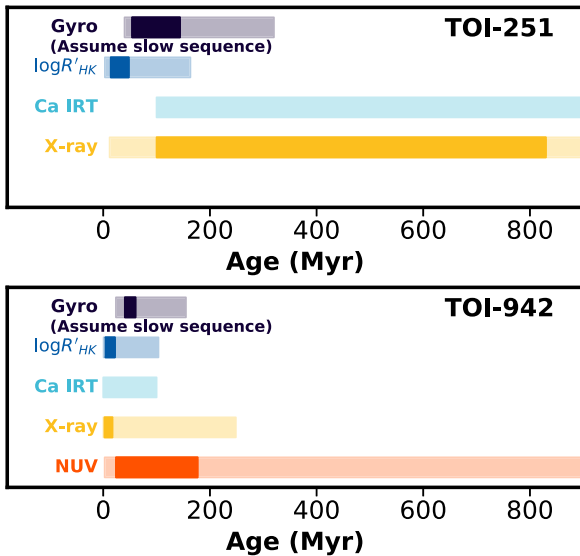


Figure 18. Summary of the age–activity indicators for TOI-251 and TOI-942. The 1σ (darker) and 3σ (lighter) age ranges from gyrochronology and spectroscopic and photometric activity indicators are marked. We adopt a final age estimate for TOI-251 of 40–320 Myr and for TOI-942 of 20–160 Myr.

4.5. Summary of Age Estimates

Figure 18 summarizes the ages of TOI-251 and TOI-942 as estimated from the age indicators. For TOI-251, gyrochronology and chromospheric Ca II HK emissions provide constraining age estimates. We adopt an estimated age range of 40–320 Myr for TOI-251, encompassing the 3σ upper range of both gyrochronology relationships we tested, and the upper limit of chromospheric Ca II HK emission estimates—the two age indicators that yielded constraining estimates in our analysis. This age range also agrees with the estimates from the less constraining Ca II infrared triplet and X-ray emission estimates, which put the age of TOI-251 below 1 Gyr.

Clearly, TOI-942 is more active than TOI-251 and members of the Pleiades cluster. Constraining measurements for the age of TOI-251 come from gyrochronology, Ca II HK emissions, and the Ca II infrared triplet emissions, placing a 3σ age range at 20–160 Myr. The age estimates from X-ray and NUV emissions are less constraining but still consistent with a young age for TOI-942. The fact that the rotation of the star is significantly slower than that of similar stars in the 13 Myr *h* Persei cluster at zero-age main sequence, and the lack of infrared excess for TOI-942, allowed us to place an approximate lower limit of 20 Myr.

5. System Modeling

To derive accurate system parameters, we present a series of global models for each system incorporating the TESS discovery light curve, ground-based follow-up light curves, radial velocities, spectroscopic and broadband atmospheric parameters, and stellar isochrone constraints.

The light curves of young stars exhibit large variations due to spot modulation. The variability signal often dwarfs the planetary transits and as such needs to be carefully considered so as to yield unbiased system parameters. The modeling of spot activity is simplified by the quasi-sinusoidal nature of the light curves, with well-defined periods that can be easily modeled. We adopt the *celerite* package (Foreman-Mackey et al. 2017) to model the stellar variability via its simple

harmonic oscillator kernel, with free parameters describing the frequency of the stellar variability $\log \omega_0 = \log 1/P_{\text{rot}}$, the dampening factor $\log Q_0$, and the power of the oscillator $\log S_0$. We impose a Gaussian prior on $\log \omega_0$ based on the rotation period of each star, with the specific limits shown in Table 5. Linear uniform priors were imposed for $\log Q_0$ and $\log S_0$. The follow-up light curves are also included in the global analysis. These light curves are not modeled as part of the Gaussian process. To account for any environmental systematics in the light curves, we instead include a linear trend for each transit, a linear coefficient detrending against airmass, and an additional offset term for meridian flips.

The transits are modeled via the *batman* package (Kreidberg 2015), with free parameters defining the period P , transit center ephemeris T_c , planet–star radius ratio R_p/R_* , and line-of-sight inclination i for each transiting planet. Limb-darkening parameters are interpolated from Claret & Bloemen (2011) and Claret (2017) and fixed through the modeling process. The radial velocities are further modeled by circular orbits, with masses of each planet m_p and a jitter term σ_{rv} to account for the radial velocity jitter. Given the large stellar activity–induced jitter for these young stars, we only provide upper limits on the masses of the planets reported here.

In addition, we model the stellar parameters simultaneously with the transits and radial velocities. The stellar properties are modeled via MESA Isochrones & Stellar Tracks (MIST; Dotter 2016) interpolated using stellar evolution tracks with ages below 1 Gyr and initial masses $0.6 M_\odot < M_* < 1.6 M_\odot$. Free parameters include the stellar mass M_* , radius R_* , and stellar metallicity $[M/H]$. These are constrained by the spectroscopic effective temperature T_{eff} , surface gravity $\log g_*$, and metallicity as measured by SPC from the TRES spectra. We also incorporate photometric magnitudes from visual Hipparcos (Perryman et al. 1997), Gaia (Gaia Collaboration et al. 2018b), and near-infrared Two Micron All Sky Survey (2MASS) bands (Skrutskie et al. 2006) in the modeling of the SED. We incorporate debiased Gaia DR2 distance estimates from Bailer-Jones et al. (2018) into the SED analysis. Though we have estimates of the stellar age, we apply no age prior to the stellar evolution modeling beyond limiting the ages to below 1 Gyr. The resulting age posteriors are largely uninformative, allowing for all ages within the given range.

The final parameters for the host stars are presented in Table 4, and the planet properties are presented in Table 5. The SEDs are shown in Figure 19, with the best-fit atmospheric model overlaid.

6. Discussion

We report the discovery and validation of planets around TOI-251 and TOI-942. The two systems of small planets are orbiting relatively young field stars, with TOI-251 estimated to be 40–320 Myr old and TOI-942 at 20–160 Myr old. The mini-Neptune TOI-251 b has an orbital period of 4.94 days and a radius of $2.74^{+0.18}_{-0.18} R_\oplus$. Two inflated Neptunes orbit TOI-942, with TOI-942b in a 4.32 day orbit with a radius of $4.81^{+0.20}_{-0.20} R_\oplus$ and TOI-942c in a 10.16 day orbit with a radius of $5.79^{+0.19}_{-0.18} R_\oplus$.

6.1. The Radius–Period Diagram for Young Planets and the Detectability of Smaller Planets

Discoveries of super-Earths and Neptunes around young stars give us a unique opportunity to explore the evolution of

Table 5
Orbital and Planetary Parameters

Parameter	TOI-251b	TOI-942b	TOI-942c
Light-curve Parameters			
P (days)	$4.937770^{+0.000028}_{-0.000029}$	$4.324190^{+0.000030}_{-0.000030}$	$10.156430^{+0.000069}_{-0.000079}$
T_c (BJD–TDB) ^a	$2,458,357.305,48^{+0.0013}_{-0.0015}$	$2,458,441.576,2^{+0.0021}_{-0.0021}$	$2,458,447.056,3^{+0.0023}_{-0.0023}$
T_{14} (days) ^a	$0.0930^{+0.0026}_{-0.0020}$	$0.1418^{+0.0025}_{-0.0018}$	$0.07994^{+0.00082}_{-0.00088}$
a/R_*	$14.02^{+0.82}_{-0.61}$	$10.12^{+0.13}_{-0.18}$	$17.88^{+0.22}_{-0.32}$
R_p/R_*	$0.02858^{+0.0011}_{-0.0010}$	$0.04322^{+0.0015}_{-0.0016}$	$0.05202^{+0.0012}_{-0.0013}$
$b \equiv a \cos i/R_*$	$0.607^{+0.047}_{-0.070}$	$0.05^{+0.05}_{-0.04}$	$0.149^{+0.119}_{-0.093}$
i (deg)	$87.52^{+0.40}_{-0.31}$	$89.97^{+0.34}_{-0.51}$	$89.54^{+0.68}_{-0.42}$
Limb- and Gravity-darkening Coefficients^b			
a'_l	0.3817
b'_l	0.3393
a_y	0.1428
b_y	0.3642
a_{MEarth}	0.1925	0.3201	...
b_{MEarth}	0.3552	0.2797	...
a_{TESS}	0.2831	0.4006	...
b_{TESS}	0.2873	0.2243	...
RV Parameters			
K (m s ⁻¹)	<120	<370	<284
e	0 (fixed)	0 (fixed)	0 (fixed)
RV jitter (m s ⁻¹)	81^{+34}_{-22}	86^{+56}_{-29}	...
Gaussian Process Hyperparameters			
log ω_0 SHOT frequency	$-1.26^{+0.14}_{-0.14}$ (Gaussian prior $\mu = -1.35$, $\sigma = 0.13$)	$-1.19^{+0.11}_{-0.11}$ (Gaussian prior $\mu = -1.22$, $\sigma = 0.11$)	...
log Q_0 SHOT quality factor	$-0.55^{+0.57}_{-0.40}$	$-1.10^{+0.43}_{-0.31}$...
log S_0 SHOT S	$-4.25^{+0.56}_{-0.56}$	$-2.37^{+0.48}_{-0.50}$...
Planetary Parameters			
R_p (R_\oplus)	$2.74^{+0.18}_{-0.18}$	$4.81^{+0.20}_{-0.20}$	$5.79^{+0.19}_{-0.18}$
M_p (M_{Jup})	<1.0	<2.6	<2.5
a (au)	$0.05741^{+0.00023}_{-0.00017}$	$0.04796^{+0.00073}_{-0.00065}$	$0.0847^{+0.0012}_{-0.0011}$

Notes.

^a T_c : Reference epoch of mid-transit that minimizes the correlation with the orbital period. T_{14} : total transit duration, time between first and last contact.

^b Values for a quadratic law given separately for each of the filters with which photometric observations were obtained. These values were adopted from the tabulations by Claret & Bloemen (2011) according to the spectroscopic initial estimate of the stellar parameters.

small planets in their early stages of evolution. Figure 20 shows the period–radius distribution of close-in small planets, comparing the planets characterized by the Kepler survey and those subsequently discovered around stars younger than 500 Myr. Photoevaporation is key in sculpting this distribution, creating a sub-Saturn desert devoid of close-in Neptunes and super-Earths (e.g., Lopez et al. 2012; Owen & Wu 2013; Owen & Lai 2018) and carving the radius valley between rocky and gaseous planets further out (e.g., Fulton et al. 2017; Owen & Wu 2017).

The planet TOI-251b straddles the evaporation gap between solid cores and planets still retaining their gaseous envelopes. It is among the smallest planets known around stars younger than 500 Myr; only the planets around the Ursa Major moving group member TOI-1726 (Mann et al. 2020) are smaller. The planets around TOI-942 lie in the sub-Saturn radius regime, similar in radii and periods to other young planetary systems at the ~ 20 –50 Myr age regime, such as DS Tuc Ab (Newton et al. 2019) and V1298 Tau c and d (David et al. 2019b).

The planets around TOI-251 and TOI-942, as well as most other planets found around young stars, have larger radii than most in the Kepler sample. However, it may be difficult to compare this sample of planets around young, active stars

against those identified by the Kepler sample around quiet stars with higher-precision light curves.

To see if smaller planets could be recovered from similar light curves, we performed a signal injection and recovery exercise on the TESS observations of TOI-251 and TOI-942. Figure 20 shows the detection thresholds derived from 1000 injected planets across the radius–period space. Each injection is drawn from a uniform distribution in period between 1 and 15 days, radius from 0.5 to 15 R_\oplus , and impact parameter from zero to 1. A circular orbit is assumed for every injected planet. The light curves are then detrended via a cosine-filtering (Mazeh & Faigler 2010) algorithm, and the transits are recovered via a box least-squares algorithm (BLS; Kovács et al. 2002) search. The injection and recovery exercise shows that the planets we discovered are nearly the smallest detectable planets. The detection thresholds worsen significantly for planets in orbits longer than 10 days. Importantly, the predominant population of close-in small planets with $R_p < 2 R_\oplus$ and those with $R_p < 3 R_\oplus$ and orbital periods > 10 days would not be detectable around either star. Similar injection and recovery exercises of previous analyses (e.g., Newton et al. 2019; Rizzuto et al. 2020) show similar results, that our detectability for planets smaller than ~ 2 –3 R_\oplus is only complete at periods shorter than 10 days.

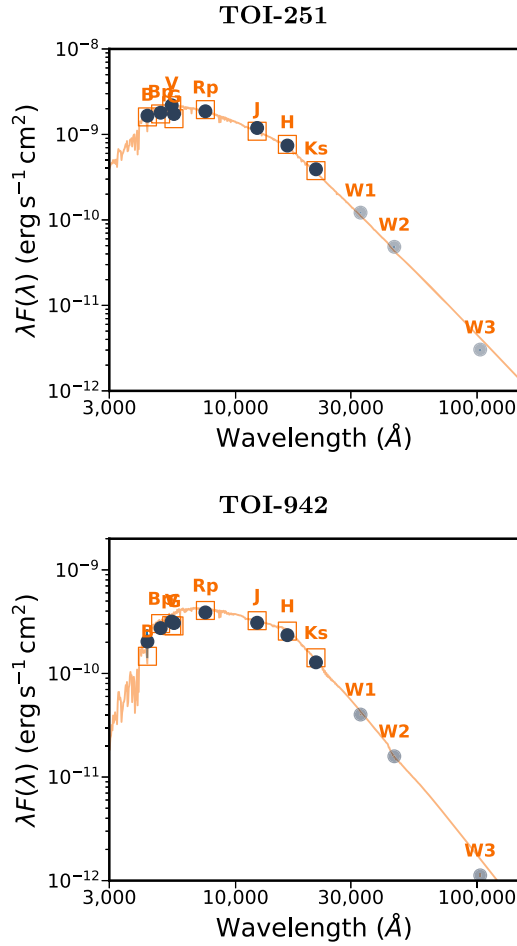


Figure 19. The SEDs of TOI-251 and TOI-942 over the Hipparcos (Perryman et al. 1997), Gaia (Gaia Collaboration et al. 2018b), and 2MASS (Skrutskie et al. 2006) bands are plotted in navy. The MIST isochrone-predicted fluxes in each band are marked by the open orange squares. The best-fit ATLAS9 (Castelli & Kurucz 2004) synthetic atmosphere model is overlaid in orange. The WISE W_1 , W_2 , and W_3 fluxes of the target stars are also shown, though they are not used to constrain the SED model.

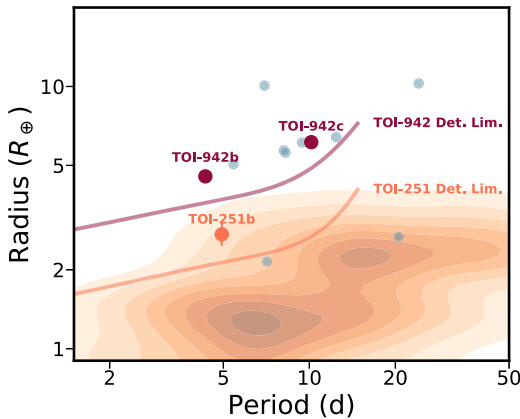


Figure 20. Period–radius distribution of close-in small planets. The contours mark the distribution of planets from the Kepler survey characterized in Fulton et al. (2017), with a gap between rocky and gaseous enveloped planets clearly seen. Planets around TOI-251 and TOI-942 are marked. The detection limits of planets around each of these stars are marked by horizontal lines. Planets around stars younger than 500 Myr old are shown by cyan points, including the planets around V1298 (David et al. 2019a, 2019b), K2-33b (David et al. 2016; Mann et al. 2016b), DS Tuc Ab (Newton et al. 2019), Kepler-63 b (Sanchis-Ojeda et al. 2013), HIP 67522b (Rizzuto et al. 2020), and TOI-1726b and c (Mann et al. 2020).

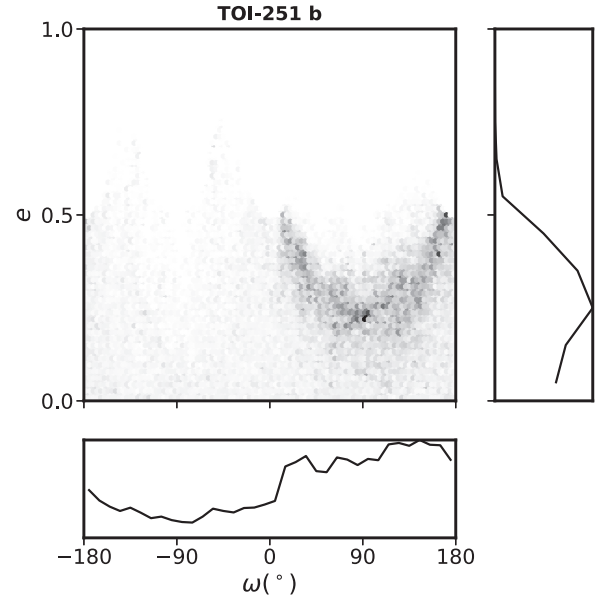


Figure 21. Eccentricity posterior for TOI-251b, as constrained by the TESS transit duration and inferred stellar parameters. We find that the eccentricity of TOI-251b can only be loosely constrained to $e < 0.64$ at 3σ significance.

6.2. Orbital Eccentricity and Prospects for Obliquity Measurements

One main tracer for the origins of close-in planets is the properties of the orbits they currently inhabit. High eccentricity or highly oblique orbits can be indicative of strong dynamical interaction in the early history of these planets.

We modified our analysis (Section 5) to allow eccentricity, modeled as $\sqrt{e} \cos \omega$ and $\sqrt{e} \sin \omega$, to be free during the global modeling. To prevent the large jitter of radial velocities and systematic effects from ground-based transit observations from influencing our eccentricity estimates, we make use of only the TESS light curves and the SED in this analysis.

Figures 21 and 22 show the resulting posteriors in eccentricity e and longitude of periastron ω . For both systems, the eccentricity can only be loosely constrained with existing data sets. We find 3σ upper limits $e < 0.64$ for TOI-251b, < 0.87 for TOI-942b, and < 0.80 for TOI-942c.

Given the difficulty in measuring precise radial velocity orbits for these planets around young, active stars, a potentially easier observational constraint on their dynamical histories is their projected orbital obliquity angles. The obliquity angle is the relative angle between the orbital planes of the planets and the rotation axis of the host star. Planets that experienced significant dynamical interactions in their past can often be found in highly oblique orbits (e.g., Triaud 2018).

The line-of-sight inclination of the host stars can be used to approximate the orbital obliquity for the planets. Following Masuda & Winn (2020), we compute the stellar inclination angle I_* via the isochrone-derived stellar radius R_* , the spectroscopic rotational broadening velocity $v \sin I_*$, and the photometric rotation period P_{rot} of each system. Though tight constraints cannot be placed with our existing observations, TOI-251 and TOI-942 appear to be well aligned, with 3σ lower limits of $I_* > 45^\circ$ for both stars (see Table 4 for their precisely derived values).

A much more precise technique of measuring the orbital obliquities of these transiting systems is to observe their

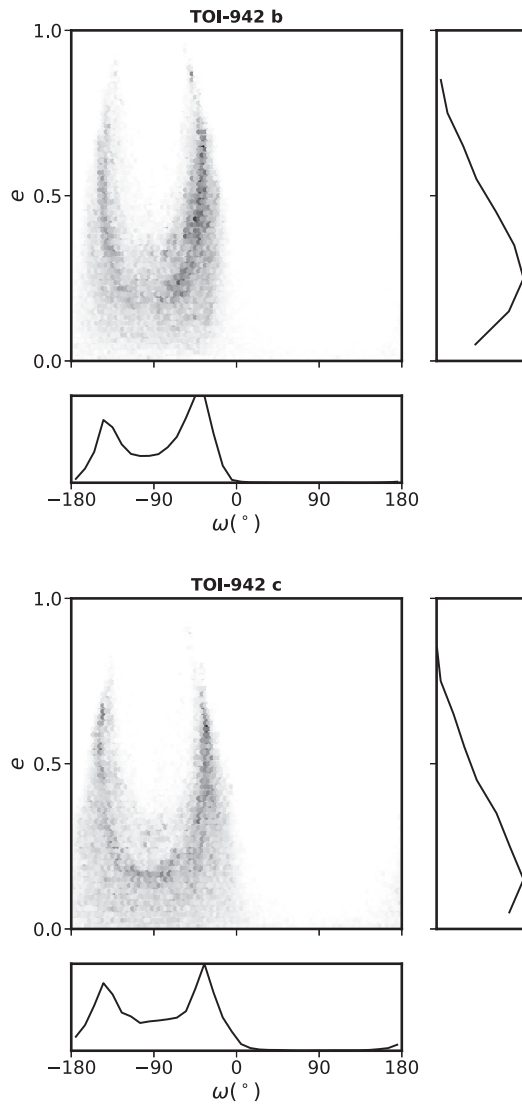


Figure 22. Eccentricity posteriors for TOI-942b and c based on their TESS transit durations and inferred host star parameters. The eccentricities are poorly constrained with existing observations, with only highly eccentric orbits ruled out. The eccentricity of TOI-942b is constrained to be $e < 0.87$, and it is $e < 0.80$ for TOI-942c at 3σ significance.

spectroscopic transits via the Rossiter–McLaughlin (McLaughlin 1924; Rossiter 1924) effect or via Doppler tomographic transit shadow detection (Donati et al. 1997; Collier Cameron et al. 2010). Based on our measured rotational broadening velocity, TOI-251b should exhibit an in-transit velocity anomaly of $\sim 4 \text{ m s}^{-1}$, while TOI-942b and TOI-942c should exhibit significant velocity variations at levels of 20–30 m s^{-1} . Planets around bright, young, rapidly rotating stars are good targets for mapping the orbital obliquity–age relationship and determining the origins of the abundance of small planets around Sun-like stars.

7. Conclusions

The two field stars TOI-251 and TOI-942 exhibit photometric and spectroscopic signatures of youth, hosting transiting Neptunes that were identified by TESS observations.

The planet TOI-251b is a $2.74_{-0.18}^{+0.18} R_{\oplus}$ mini-Neptune in a 4.94 day period around a G-type star. The period and transit ephemeris of the system were refined by three ground-based

follow-up observations that successfully detected the 1 mmag transit events on the target star. We were able to eliminate false-positive scenarios with extensive spectroscopic follow-up and speckle imaging of the host star, validating the planetary nature of the transits.

We estimated the age of TOI-251 to be 40–320 Myr based on its photometric rotation period, its spectroscopic Ca II core emission in the HK and infrared triplet lines, and the presence of X-ray emission from the ROSAT all-sky survey. The rotation period and 6708 Å lithium absorption strength are comparable to those of stars in the Pleiades cluster, agreeing with our age estimates for the system.

The star TOI-942 hosts two Neptune-sized planets around a K-type star. The planet TOI-942b is a $4.81_{-0.20}^{+0.20} R_{\oplus}$ planet in a 4.32 day period orbit, while TOI-942c has a radius of $5.79_{-0.18}^{+0.19} R_{\oplus}$ and an orbital period of 10.16 days. The transits of TOI-942b and c were both successfully recovered by an extensive ground-based follow-up campaign with the MEarth telescope array. The planetary nature of the system was further validated by diffraction-limited imaging and spectroscopic analyses.

The age of TOI-942 is significantly younger than that of TOI-251, estimated at 20–160 Myr. It exhibits strong X-ray and calcium emission that are stronger and beyond the range of calibrated literature age–activity relationships. The rotation period and lithium absorption strength of TOI-942 suggest that it has an age younger than the Pleiades cluster and more in agreement with younger stellar associations.

Both TOI-251 and TOI-942 are examples of young planet-hosting field stars that can contribute significantly to characterizing the relationship between planet properties and their ages. TESS is likely to yield numerous systems like TOI-251 and TOI-942 that are amenable to extensive follow-up observations that can characterize the orbital and atmospheric properties of planets at early stages of their evolution.

The authors became aware of a parallel effort on the characterization of TOI-942 by Carleo et al. in the late stages of the manuscript preparations. The submissions are coordinated, and no analyses or results were shared prior to submission.















Work by G.Z. is supported by NASA through Hubble Fellowship grant HST-HF2-51402.001-A awarded by the Space Telescope Science Institute, which is operated by the Association of Universities for Research in Astronomy, Inc., for NASA, under contract NAS 5-26555. The MEarth Team gratefully acknowledges funding from the David and Lucile Packard Fellowship for Science and Engineering (awarded to D.C.). This material is based upon work supported by the National Science Foundation under grants AST-0807690, AST-1109468, AST-1004488 (Alan T. Waterman Award), and AST-1616624 and the National Aeronautics and Space Administration under grant No. 80NSSC18K0476 issued through the XRP Program. This work is made possible by a grant from the John Templeton Foundation. The opinions expressed in this publication are those of the authors and do not necessarily reflect the views of the John Templeton Foundation. This research has made use of the NASA Exoplanet Archive, which is operated by the California Institute of Technology, under contract with the National Aeronautics and Space Administration under the Exoplanet Exploration Program. Funding for the TESS mission is provided by NASA’s Science Mission directorate. We acknowledge the use of public









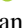















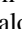



TESS Alert data from pipelines at the TESS Science Office and the TESS Science Processing Operations Center. This research has made use of the Exoplanet Follow-up Observation Program website, which is operated by the California Institute of Technology, under contract with the National Aeronautics and Space Administration under the Exoplanet Exploration Program. This paper includes data collected by the TESS mission that are publicly available from the Mikulski Archive for Space Telescopes (MAST). Resources supporting this work were provided by the NASA High-End Computing (HEC) Program through the NASA Advanced Supercomputing (NAS) Division at Ames Research Center for the production of the SPOC data products. This work makes use of data from the Mount Wilson HK Project. The HK_Project_v1995_NSO data derive from the Mount Wilson Observatory HK Project, which was supported by both public and private funds through the Carnegie Observatories, the Mount Wilson Institute, and the Harvard-Smithsonian Center for Astrophysics starting in 1966 and continuing for over 36 yr. These data are the result of the dedicated work of O. Wilson, A. Vaughan, G. Preston, D. Duncan, S. Baliunas, and many others. This work makes use of observations from the LCOGT network. Some of the observations in the paper made use of the high-resolution imaging instrument(s) Alopeke (and/or Zorro). Alopeke (and/or Zorro) was funded by the NASA Exoplanet Exploration Program and built at the NASA Ames Research Center by Steve B. Howell, Nic Scott, Elliott P. Horch, and Emmett Quigley. Alopeke (and/or Zorro) was mounted on the Gemini-North (and/or South) telescope of the international Gemini Observatory, a program of NOIRLab, which is managed by the Association of Universities for Research in Astronomy (AURA) under a cooperative agreement with the National Science Foundation on behalf of the Gemini partnership: the National Science Foundation (United States), National Research Council (Canada), Agencia Nacional de Investigación y Desarrollo (Chile), Ministerio de Ciencia, Tecnología e Innovación (Argentina), Ministério da Ciência, Tecnologia, Inovação e Comunicação (Brazil), and Korea Astronomy and Space Science Institute (Republic of Korea).

Facilities: FLWO 1.5 m, CHIRON, TESS, LCOGT, MEarth, Gemini, Subaru.

Software: lightkurve (Barentsen et al. 2019), emcee (Foreman-Mackey et al. 2013), Astropy (Astropy Collaboration et al. 2013, 2018), AstroImageJ (Collins et al. 2017), PyAstronomy (Czesla et al. 2019), TESSCut (Brasseur et al. 2019).

ORCID iDs

George Zhou  <https://orcid.org/0000-0002-4891-3517>
 Samuel N. Quinn  <https://orcid.org/0000-0002-8964-8377>
 Chelsea X. Huang  <https://orcid.org/0000-0003-0918-7484>
 Karen A. Collins  <https://orcid.org/0000-0001-6588-9574>
 Luke G. Bouma  <https://orcid.org/0000-0002-0514-5538>
 Andrew M. Vanderburg  <https://orcid.org/0000-0001-7246-5438>
 Joseph E. Rodriguez  <https://orcid.org/0000-0001-8812-0565>
 David W. Latham  <https://orcid.org/0000-0001-9911-7388>
 Guillermo Torres  <https://orcid.org/0000-0002-5286-0251>
 Stephanie T. Douglas  <https://orcid.org/0000-0001-7371-2832>
 Allyson Bieryla  <https://orcid.org/0000-0001-6637-5401>
 Gilbert A. Esquerdo  <https://orcid.org/0000-0002-9789-5474>
 Michael L. Calkins  <https://orcid.org/0000-0002-2830-5661>
 Lars A. Buchhave  <https://orcid.org/0000-0003-1605-5666>

David Charbonneau  <https://orcid.org/0000-0002-9003-484X>
 Kevin I. Collins  <https://orcid.org/0000-0003-2781-3207>
 John F. Kielkopf  <https://orcid.org/0000-0003-0497-2651>
 Eric L. N. Jensen  <https://orcid.org/0000-0002-4625-7333>
 Thiam-Guan Tan  <https://orcid.org/0000-0001-5603-6895>
 Christopher Stockdale  <https://orcid.org/0000-0003-2163-1437>
 Carl Ziegler  <https://orcid.org/0000-0002-0619-7639>
 Nicholas Law  <https://orcid.org/0000-0001-9380-6457>
 Andrew W. Mann  <https://orcid.org/0000-0003-3654-1602>
 Steve B. Howell  <https://orcid.org/0000-0002-2532-2853>
 Rachel A. Matson  <https://orcid.org/0000-0001-7233-7508>
 Nicholas J. Scott  <https://orcid.org/0000-0003-1038-9702>
 Elise Furlan  <https://orcid.org/0000-0001-9800-6248>
 Russel J. White  <https://orcid.org/0000-0001-5313-7498>
 Coel Hellier  <https://orcid.org/0000-0002-3439-1439>
 David R. Anderson  <https://orcid.org/0000-0001-7416-7522>
 George Ricker  <https://orcid.org/0000-0003-2058-6662>
 Roland Vanderspek  <https://orcid.org/0000-0001-6763-6562>
 Sara Seager  <https://orcid.org/0000-0002-6892-6948>
 Jon M. Jenkins  <https://orcid.org/0000-0002-4715-9460>
 Joshua N. Winn  <https://orcid.org/0000-0002-4265-047X>
 Ismael Mireles  <https://orcid.org/0000-0002-4510-2268>
 Pamela Rowden  <https://orcid.org/0000-0002-4829-7101>
 Daniel A. Yahalomi  <https://orcid.org/0000-0003-4755-584X>
 Bill Wohler  <https://orcid.org/0000-0002-5402-9613>
 Clara E. Brasseur  <https://orcid.org/0000-0002-9314-960X>
 Tansu Daylan  <https://orcid.org/0000-0002-6939-9211>
 Knicole D. Colón  <https://orcid.org/0000-0001-8020-7121>

References

- Astropy Collaboration, Price-Whelan, A. M., Sipőcz, B. M., et al. 2018, *AJ*, **156**, 123
- Astropy Collaboration, Robitaille, T. P., Tollerud, E. J., et al. 2013, *A&A*, **558**, A33
- Bailer-Jones, C. A. L., Rybizki, J., Fouesneau, M., Mantelet, G., & Andrae, R. 2018, *AJ*, **156**, 58
- Baliunas, S. L., Donahue, R. A., Soon, W. H., et al. 1995, *ApJ*, **438**, 269
- Barentsen, G., Hedges, C., Vinícius, Z., et al. 2019, KeplerGO/lightkurve: Lightkurve v1.0b29 (Version v1.0b29), Zenodo, doi:10.5281/zenodo.2565212
- Barnes, S. A. 2007, *ApJ*, **669**, 1167
- Bell, C. P. M., Murphy, S. J., & Mamajek, E. E. 2017, *MNRAS*, **468**, 1198
- Berta, Z. K., Irwin, J., Charbonneau, D., Burke, C. J., & Falco, E. E. 2012, *AJ*, **144**, 145
- Bianchi, L., Shiao, B., & Thilker, D. 2017, *ApJS*, **230**, 24
- Bouma, L. G., Hartman, J. D., Bhatti, W., Winn, J. N., & Bakos, G. Á. 2019, *ApJS*, **245**, 13
- Brasseur, C. E., Phillip, C., Fleming, S. W., Mullally, S. E., & White, R. L. 2019, Astrocut: Tools for Creating Cutouts of TESS Images, v0.1, Astrophysics Source Code Library, ascl:1905.007
- Brown, T. M., Baliber, N., Bianco, F. B., et al. 2013, *PASP*, **125**, 1031
- Buchhave, L. A., Bakos, G. Á., Hartman, J. D., et al. 2010, *ApJ*, **720**, 1118
- Buchhave, L. A., Latham, D. W., Johansen, A., et al. 2012, *Natur*, **486**, 375
- Cantat-Gaudin, T., Jordi, C., Vallenari, A., et al. 2018, *A&A*, **618**, A93
- Cantat-Gaudin, T., Jordi, C., Wright, N. J., et al. 2019, *A&A*, **626**, A17
- Castelli, F., & Kurucz, R. L. 2004, arXiv:astro-ph/0405087
- Ciardi, D. R., Crossfield, I. J. M., Feinstein, A. D., et al. 2018, *AJ*, **155**, 10
- Claret, A. 2017, *A&A*, **600**, A30
- Claret, A., & Bloemen, S. 2011, *A&A*, **529**, A75
- Collier Cameron, A., Guenther, E., Smalley, B., et al. 2010, *MNRAS*, **407**, 507
- Collins, K. A., Kielkopf, J. F., Stassun, K. G., & Hessman, F. V. 2017, *AJ*, **153**, 77
- Cutri, R. M., Wright, E. L., Conrow, T., et al. 2014, *yCat*, **2328**, 0

- Czesla, S., Schröter, S., Schneider, C. P., et al. 2019, PyA: Python Astronomy-related Packages, v0.15.2, Astrophysics Source Code Library, ascl:1906.010
- Damiani, F., Prisinzano, L., Pillitteri, I., Micela, G., & Sciortino, S. 2019, *A&A*, **623**, A112
- David, T. J., Cody, A. M., Hedges, C. L., et al. 2019a, *AJ*, **158**, 79
- David, T. J., Crossfield, I. J. M., Benneke, B., et al. 2018a, *AJ*, **155**, 222
- David, T. J., Hillenbrand, L. A., Petigura, E. A., et al. 2016, *Natur*, **534**, 658
- David, T. J., Mamajek, E. E., Vanderburg, A., et al. 2018b, *AJ*, **156**, 302
- David, T. J., Petigura, E. A., Luger, R., et al. 2019b, *ApJL*, **885**, L12
- Dias, W. S., Monteiro, H., Caetano, T. C., et al. 2014, *A&A*, **564**, A79
- Donati, J.-F., Semel, M., Carter, B. D., Rees, D. E., & Collier Cameron, A. 1997, *MNRAS*, **291**, 658
- Dotter, A. 2016, *ApJS*, **222**, 8
- Douglas, S. T., Agüeros, M. A., Covey, K. R., et al. 2016, *ApJ*, **822**, 47
- Duncan, D. K., Vaughan, A. H., Wilson, O. C., et al. 1991, *ApJS*, **76**, 383
- Fűrész, G. 2008, PhD thesis, Univ. of Szeged
- Findeisen, K., Hillenbrand, L., & Soderblom, D. 2011, *AJ*, **142**, 23
- Fleming, T. A., Schmitt, J. H. M. M., & Giampapa, M. S. 1995, *ApJ*, **450**, 401
- Foreman-Mackey, D., Agol, E., Angus, R., & Ambikasaran, S. 2017, *AJ*, **154**, 220
- Foreman-Mackey, D., Hogg, D. W., Lang, D., & Goodman, J. 2013, *PASP*, **125**, 306
- Fulton, B. J., Petigura, E. A., Howard, A. W., et al. 2017, *AJ*, **154**, 109
- Gagné, J., & Faherty, J. K. 2018, *ApJ*, **862**, 138
- Gagné, J., Mamajek, E. E., Malo, L., et al. 2018a, *ApJ*, **856**, 23
- Gagné, J., Roy-Loubier, O., Faherty, J. K., Doyon, R., & Malo, L. 2018b, *ApJ*, **860**, 43
- Gaia Collaboration, Babusiaux, C., van Leeuwen, F., et al. 2018a, *A&A*, **616**, A10
- Gaia Collaboration, Brown, A. G. A., Vallenari, A., et al. 2018b, *A&A*, **616**, A1
- Gray, D. F. 2005, *The Observation and Analysis of Stellar Photospheres* (3rd ed.; Cambridge: Cambridge Univ. Press)
- Green, G. 2018, *JOSS*, **3**, 695
- Green, G. M., Schlafly, E., Zucker, C., Speagle, J. S., & Finkbeiner, D. 2019, *ApJ*, **887**, 93
- Høg, E., Fabricius, C., Makarov, V. V., et al. 2000, *A&A*, **355**, L27
- Howell, S. B., Everett, M. E., Horch, E. P., et al. 2016, *ApJL*, **829**, L2
- Howell, S. B., Everett, M. E., Sherry, W., Horch, E., & Ciardi, D. R. 2011, *AJ*, **142**, 19
- Huang, X., Burt, J., Vanderburg, A., et al. 2019, AAS Meeting, **233**, 209.08
- Irwin, J., Irwin, M., Aigrain, S., et al. 2007, *MNRAS*, **375**, 1449
- Irwin, J. M., Berta-Thompson, Z. K., Charbonneau, D., et al. 2015, in 18th Cambridge Workshop on Cool Stars, Stellar Systems, and the Sun, ed. G. van Belle & H. C. Harris (Flagstaff, AZ: Lowell Observatory), 767
- Jenkins, J. M., Twicken, J. D., McCauliff, S., et al. 2016, *Proc. SPIE*, **9913**, 99133E
- Jensen, E. 2013, Tapir: A Web Interface for Transit/Eclipse Observability, Astrophysics Source Code Library, ascl:1306.007
- Kharchenko, N. V., Piskunov, A. E., Schilbach, E., Rser, S., & Scholz, R.-D. 2013, *A&A*, **558**, A53
- Kounkel, M., & Covey, K. 2019, *AJ*, **158**, 122
- Kovács, G., Zucker, S., & Mazeh, T. 2002, *A&A*, **391**, 369
- Kraus, A. L., Shkolnik, E. L., Allers, K. N., & Liu, M. C. 2014, *AJ*, **147**, 146
- Kreidberg, L. 2015, *PASP*, **127**, 1161
- Krumholz, M. R., McKee, C. F., & Bland-Hawthorn, J. 2019, *ARA&A*, **57**, 227
- Li, J., Tenenbaum, P., Twicken, J. D., et al. 2019, *PASP*, **131**, 024506
- Livingston, J. H., Dai, F., Hirano, T., et al. 2018, *AJ*, **155**, 115
- Livingston, J. H., Dai, F., Hirano, T., et al. 2019, *MNRAS*, **484**, 8
- Lodieu, N., Pérez-Garrido, A., Smart, R. L., & Silvotti, R. 2019, *A&A*, **628**, A66
- Lopez, E. D., Fortney, J. J., & Miller, N. 2012, *ApJ*, **761**, 59
- Mamajek, E. E. 2009, in AIP Conf. Ser. 1158, *Exoplanets and Disks: Their Formation and Diversity*, ed. T. Usuda, M. Tamura, & M. Ishii (Melville, NY: AIP), 3
- Mamajek, E. E., & Hillenbrand, L. A. 2008, *ApJ*, **687**, 1264
- Mann, A. W., Gaidos, E., Mace, G. N., et al. 2016a, *ApJ*, **818**, 46
- Mann, A. W., Gaidos, E., Vanderburg, A., et al. 2017, *AJ*, **153**, 64
- Mann, A. W., Johnson, M. C., Vanderburg, A., et al. 2020, *AJ*, **160**, 179
- Mann, A. W., Newton, E. R., Rizzuto, A. C., et al. 2016b, *AJ*, **152**, 61
- Mann, A. W., Vanderburg, A., Rizzuto, A. C., et al. 2018, *AJ*, **155**, 4
- Masuda, K., & Winn, J. N. 2020, *AJ*, **159**, 81
- Mazeh, T., & Faigler, S. 2010, *A&A*, **521**, L59
- McCully, C., Volgenau, N. H., Harbeck, D.-R., et al. 2018, *Proc. SPIE*, **10707**, 107070K
- McLaughlin, D. B. 1924, *ApJ*, **60**, 22
- Montet, B. T., Feinstein, A. D., Luger, R., et al. 2020, *AJ*, **159**, 112
- Morax, E., Artemenko, S., Bouvier, J., et al. 2013, *A&A*, **560**, A13
- Morris, R. L., Twicken, J. D., Smith, J. C., et al. 2020, *Kepler Data Processing Handbook: Photometric Analysis*, Kepler Data Processing Handbook KSCI-19081-003
- Newton, E. R., Mann, A. W., Tofflemire, B. M., et al. 2019, *ApJL*, **880**, L17
- Noyes, R. W., Hartmann, L. W., Baliunas, S. L., Duncan, D. K., & Vaughan, A. H. 1984, *ApJ*, **279**, 763
- Obermeier, C., Henning, T., Schlieder, J. E., et al. 2016, *AJ*, **152**, 223
- Oh, S., Price-Whelan, A. M., Hogg, D. W., Morton, T. D., & Spergel, D. N. 2017, *AJ*, **153**, 257
- Owen, J. E., & Lai, D. 2018, *MNRAS*, **479**, 5012
- Owen, J. E., & Wu, Y. 2013, *ApJ*, **775**, 105
- Owen, J. E., & Wu, Y. 2017, *ApJ*, **847**, 29
- Perryman, M. A. C., Lindegren, L., Kovalevsky, J., et al. 1997, *A&A*, **500**, 501
- Plavchan, P., Barclay, T., & Gagné, J. 2020, *Natur*, **582**, 497
- Pollacco, D. L., Skillen, I., Collier Cameron, A., et al. 2006, *PASP*, **118**, 1407
- Quinn, S. N., White, R. J., Latham, D. W., et al. 2012, *ApJL*, **756**, L33
- Quinn, S. N., White, R. J., Latham, D. W., et al. 2014, *ApJ*, **787**, 27
- Randich, S., Aharpour, N., Pallavicini, R., Prosser, C. F., & Stauffer, J. R. 1997, *A&A*, **323**, 86
- Randich, S., Pallavicini, R., Meola, G., Stauffer, J. R., & Balachandran, S. C. 2001, *A&A*, **372**, 862
- Rebull, L. M., Stauffer, J. R., Bouvier, J., et al. 2016, *AJ*, **152**, 113
- Rebull, L. M., Stauffer, J. R., Hillenbrand, L. A., et al. 2017, *ApJ*, **839**, 92
- Ricker, G. R., Vanderspek, R., Winn, J., et al. 2016, *Proc. SPIE*, **9904**, 99042B
- Rizzuto, A. C., Ireland, M. J., & Robertson, J. G. 2011, *MNRAS*, **416**, 3108
- Rizzuto, A. C., Mann, A. W., Vanderburg, A., Kraus, A. L., & Covey, K. R. 2017, *AJ*, **154**, 224
- Rizzuto, A. C., Newton, E. R., Mann, A. W., et al. 2020, *AJ*, **160**, 33
- Rizzuto, A. C., Vanderburg, A., Mann, A. W., et al. 2018, *AJ*, **156**, 195
- Rosat, C. 2000, *yCat*, **9030**, 0
- Röser, S., Schilbach, E., Piskunov, A. E., Kharchenko, N. V., & Scholz, R.-D. 2011, *A&A*, **531**, A92
- Rossiter, R. A. 1924, *ApJ*, **60**, 15
- Sanchis-Ojeda, R., Winn, J. N., Marcy, G. W., et al. 2013, *ApJ*, **775**, 54
- Seager, S., & Mallén-Ornelas, G. 2003, *ApJ*, **585**, 1038
- Skutskie, M. F., Cutri, R. M., Stiening, R., et al. 2006, *AJ*, **131**, 1163
- Stassun, K. G., Oelkers, R. J., Pepper, J., et al. 2018, *AJ*, **156**, 102
- Stauffer, J., Rebull, L. M., Cody, A. M., et al. 2018, *AJ*, **156**, 275
- Sullivan, P. W., Winn, J. N., Berta-Thompson, Z. K., et al. 2015, *ApJ*, **809**, 77
- Tokovinin, A. 2018, *PASP*, **130**, 035002
- Tokovinin, A., Fischer, D. A., Bonati, M., et al. 2013, *PASP*, **125**, 1336
- Triaud, A. H. M. J. 2018, in *Handbook of Exoplanets*, ed. H. Deeg & J. Belmonte (Cham: Springer), 1375
- Twicken, J. D., Catanzarite, J. H., Clarke, B. D., et al. 2018, *PASP*, **130**, 064502
- Twicken, J. D., Clarke, B. D., Bryson, S. T., et al. 2010, *Proc. SPIE*, **7740**, 774023
- Vanderburg, A., Huang, C. X., Rodriguez, J. E., et al. 2019, *ApJL*, **881**, L19
- Vanderburg, A., Mann, A. W., Rizzuto, A., et al. 2018, *AJ*, **156**, 46
- Vaughan, A. H., Preston, G. W., & Wilson, O. C. 1978, *PASP*, **90**, 267
- Voges, W., Aschenbach, B., Boller, T., et al. 2000, *yCat*, **9029**, 0
- Žerjal, M., Ireland, M. J., Nordlander, T., et al. 2019, *MNRAS*, **484**, 4591
- Žerjal, M., Zwitter, T., Matijevič, G., et al. 2013, *ApJ*, **776**, 127
- Žerjal, M., Zwitter, T., Matijevič, G., et al. 2017, *ApJ*, **835**, 61
- Williams, J. P., & Cieza, L. A. 2011, *ARA&A*, **49**, 67
- Wilson, O. C. 1978, *ApJ*, **226**, 379
- Wright, E. L., Eisenhardt, P. R. M., Mainzer, A. K., et al. 2010, *AJ*, **140**, 1868
- Zari, E., Hashemi, H., Brown, A. G. A., Jardine, K., & de Zeeuw, P. T. 2018, *A&A*, **620**, A172
- Zhou, G., Rodriguez, J. E., Vanderburg, A., et al. 2018, *AJ*, **156**, 93
- Zhou, G., Winn, J. N., Newton, E. R., et al. 2020, *ApJL*, **892**, L21
- Ziegler, C., Tokovinin, A., Briceño, C., et al. 2020, *AJ*, **159**, 19